# COMPARING COMPRESSIBILITY EFFECTS IN TURBULENCE AT VARIOUS MACH NUMBERS

A Thesis

Presented to the Faculty of the Graduate School

of Cornell University

in Partial Fulfillment of the Requirements for the Degree of

Master of Science

by

Dasha Alexandra Gloutak

December 2018

## ABSTRACT

Compressibility effects in a high speed turbulent flow were examined experimentally within a novel pressure vessel equipment setup. The equipment was assembled, validated and utilized in a series of air and $SF_6$ test cases. Using these two gases allowed Reynolds Number to be adjusted separately from Mach Number. In this way, the boundary conditions and nature of the turbulence determined by Reynolds Number were maintained, however the compressibility effects determined by Mach Number were changed. The turbulent flows consisted of a solenoidal component generated by a high speed fan and a dilatational component by high sound pressure level (SPL) speakers. Large scale turbulence dynamics, including axial, radial and power profiles, remained similar for both gas cases. However, small scale turbulence dynamics, including velocity energy spectra and velocity derivative skewness, revealed compressibility effects at work for the high speed and high SPL cases in $SF_6$.

## BIOGRAPHICAL SKETCH

Dasha Gloutak received her Bachelors of Science in Mechanical Engineering at the University of California Los Angeles in 2014. After graduating, she worked as a Mechanical Design Engineer at Northrop Grumman designing inertial navigation systems before pursuing a Masters of Science in Mechanical Engineering at Cornell University. While conducting research in the Bewley Applied Turbulence Laboratory (BATL), she also worked as a Teaching Assistant for a variety of undergraduate mechanical engineering courses, for which she received a Teaching Assistant Award from the Mechanical and Aerospace Engineering department.

This document is dedicated to Dr. Marcia Sawyer.

## ACKNOWLEDGEMENTS

This project could not have been completed without the extensive encouragement and guidance from my advisor, Dr. Greg Bewley. A special thank you to my committee member Dr. Edwin Cowen for providing great insight in my data analysis. The dedication of Master of Engineering students Armen Berberian, Drew Cohen, Tyler Green, Ben Oster, Donald Feng, and Kayla Rajsky to designing, manufacturing and testing the pressure vessel structural and operational components made this project possible. Undergraduate students Melaney Chen, Christopher Vahn, Kathryn Roberts, Alexandra Ramos Figueroa and Winnie Chan worked with great energy and enthusiasm on everything else in between. Lastly, thank you to the BATL lab for making Upson 168 a creative and innovative place to work.

## TABLE OF CONTENTS

## LIST OF TABLES

## LIST OF FIGURES

## LIST OF SYMBOLS

| | |
|---|---|
| $A$ | King's Law coefficient |
| $A_l$ | area of gas line |
| $A_f$ | area of fan |
| $a_o$ | coefficient of resistance |
| $a_w$ | wire overheat ratio |
| $B$ | King's Law coefficient |
| $c$ | speed of sound |
| $C$ | energy spectrum scaling coefficient |
| $C_d$ | discharge coefficient |
| $C_\varepsilon$ | dissipation coefficient |
| $C_f$ | fan coefficient |
| $c_p$ | specific heat for constant pressure |
| $D$ | fan diameter |
| $d_w$ | wire diameter |
| $E$ | hot wire voltage |
| $E_{11}$ | 1D energy spectra |
| $f$ | frequency |
| $F$ | force |
| $h$ | heat transfer coefficient |
| $k$ | thermal conductivity |
| $L$ | length from fan to probe mount structure |
| $l_o$ | integral length |
| $l_w$ | wire length |
| $\dot{m}$ | mass flow rate |
| $M$ | Mach Number |
| $M_t$ | turbulent Mach Number |
| $\mathcal{M}$ | molar mass of a gas |
| $n$ | King's Law coefficient |
| $n_1$ | energy spectra inertial scaling power coefficient |
| $N$ | number of samples |
| $Nu$ | Nusselt Number |
| $p$ | pressure |
| $p^*$ | critical pressure |
| $p_o$ | stagnation pressure |
| $P_f$ | fan power |
| $P_{sp}$ | speaker power |
| $Pr$ | Prandtl Number |
| $q$ | leak rate |
| $Q$ | heat transfer rate |

| | |
|---|---|
| $r$ | radial distance |
| $r_x$ | incremental axial distance |
| $R$ | gas constant |
| $R_w$ | resistance of hot wire |
| $Re$ | Reynolds Number |
| $r_{1/2}$ | radius half-width |
| $S$ | skewness |
| SPL | sound pressure level |
| $t$ | time |
| $t_{.95}$ | t-value for 95% confidence interval |
| $T$ | temperature |
| $T_w$ | wire temperature |
| $T_o$ | ambient temperature |
| $u$ | 3D fluctuating velocity |
| $u'$ | rms of 3D fluctuating velocity |
| $u_1$ | 1D component of fluctuating velocity |
| $u_1'$ | rms of 1D component of fluctuating velocity |
| $U$ | velocity |
| $\bar{U}$ | mean velocity |
| $\bar{U}_f$ | fan mean velocity at exit |
| $V$ | volume |
| $x$ | axial distance |
| $z$ | height |

| | |
|---|---|
| $\varepsilon$ | dissipation |
| $\eta$ | Kolmogorov scale |
| $\gamma$ | ratio of specific heats |
| $\kappa$ | wavenumber |
| $\lambda$ | Taylor scale |
| $\lambda_{sp}$ | speaker frequency wavelength |
| $\mu$ | dynamic viscosity |
| $\nu$ | kinematic viscosity |
| $\rho$ | density |
| $\rho_o$ | upstream stagnation density |
| $\sigma$ | standard deviation |
| $\tau$ | eddy turnover time |

CHAPTER 1

# INTRODUCTION

Compressible turbulence plays a major role in a variety of aerospace applications, including high speed commercial and military aircraft [1, 2]. These vehicles primarily operate in flow fields with steep velocity derivatives that can generate fluid pockets of different densities. The viscous boundary layer about an aircraft's fuselage and wings is one such location, where the freestream velocity transforms to a no-slip zero velocity condition at the surface [3]. Combustion processes in jet engines compress the freestream fluid in turbulent fuel-air mixing layers to create thrust [4]. The shock wave that protrudes from an aircraft's nose at supersonic speeds can adversely affect lift and drag as the shock wave interacts with aerodynamic flow over the wings [5]. These compressible turbulence phenomena have recently been attributed to cause extreme vibrations, noise, and drag effects on aircraft traveling at high speeds[2].

Studies in astrophysics have also observed compressible turbulence at work. Galactic rotations of interstellar medium, which is matter between star systems in a galaxy, dissipate energy down to the atomic viscosity scale [6]. While typical solenoidal (rotational) turbulence exhibits a 5/3 inertial range scaling in energy spectra, an added compressive component in the turbulence dissipates more energy and therefore exhibits a compressible 2 scaling in the inertial range [7]. Viscous dissipation in interstellar clouds follows this compressible inertial scaling in the energy spectra [8]. New theories have emerged that relate compressible turbulent motions such as these to the structure and formation of the universe [9].

Recent progress in studying these compressibility effects is primarily from

numerical simulations. Eddy shocklets were first proposed by Lee et al. from numerical simulations, where fluctuating fields of turbulent eddies generated shocklets that had all the characteristics of a typical shock wave [10]. Computational fluid dynamics (CFD) schemes have since been developed to resolve fluid flow dynamics around shocklets [11]. These shocklets can be identified with general dilatation criteria, and can exist even in subsonic regimes [10, 11]. Still, many computational findings have yet to be validated by experimental tests.

The original closed-circuit wind tunnels built to study experimental compressible flows were primarily used to research aerodynamic designs for aircraft. NACA Langley Research Center's 21 bar Variable Density Wind Tunnel (VDT) was used to test aircraft components in air at different atmospheric pressures [12]. The Low Turbulence Pressure Tunnel (LTPT) also at Langley was used to examine low turbulence intensity flow over airfoils at air pressures up to 16 bar [13]. The Compressed Air Tunnel at the National Physical Laboratory was used to study aerodynamics phenomena at pressures up to 25 bar [14]. At the German Aerospace Center, the Transonic Wind Tunnel (TWG) was used to research a variety of aerodynamic bodies at speeds up to Mach 1.2 in air [15, 16, 17].

A variety of compressible gas facilities were later built to specifically study turbulence. The Shock Tube Research Facility (STURF) at New York's City College was used to investigate shock propagation and grid turbulence up to 207 bar in air [18, 19]. The Southern California Co-operative Wind Tunnel was used to experiment with grid turbulence in air up to 4 bar [20]. The Princeton Super-Pipe at the Princeton Gas Dynamics Lab was used to measure scaling laws of

pipe flows of air up to 220 bar [21]. The Variable Density Wind Tunnel (VDTT) at the Max Planck Institute was used to evaluate grid turbulence using both air and sulfur hexaflouride ($SF_6$) at pressures up to 20 bar [22].

Most of these experimental facilities typically used scaled models based on Reynolds Number to maintain consistency between experiments at different air pressures. However, scaling models relative to the facility alters the experiment's boundary conditions. The objective of this experiment is to use two gases with different speeds of sound in the same experimental setup to change Mach Number independently of Reynolds Number, as determined by boundary conditions. The hypothesis of this experiment is that compressibility effects can be isolated from other experimental inputs by allowing only the Mach Number to change between experiments while keeping Reynolds Number the same. Compressibility effects on turbulent flows are determined by a higher order scaling in the inertial range of the energy spectra and overall lower absolute values of velocity derivative skewness statistics. The air and $SF_6$ cases will be compared and analyzed for these trends.

The following experimental equipment was designed to handle both air and $SF_6$, similar to the VDTT. Dense $SF_6$ gas, nearly 6 times more than air, with a similar dynamic viscosity can be used to specify the same Reynolds Number as in air with a drastically different speed of sound, nearly 2.5 times less than air. Because compressibility effects become important at higher Mach Number, the higher speed of sound in air qualifies $SF_6$ to be the compressible gas and air the incompressible gas for experiments. A high speed fan will provide solenoidal forcing on the fluid, and an additional compressive, nonrotational forcing will be imposed on the turbulent jet flow by high sound pressure level (SPL) speak-

ers. Changing the gas will alter the Mach Number on the turbulent flow imposed by the experimental setup without changing the boundary conditions set by the Reynolds Number.

CHAPTER 2

# EXPERIMENTAL SETUP

The following describes the Turbulence Research Experimental Equipment (T-RExE) setup for compressible turbulence experiments. All pressures are given in terms of absolute pressure unless otherwise specified.

## 2.1 Pressure Vessel

The 16 bar pressure vessel used in this experiment is a 1385L pressure vessel, about 1m in diameter and 3m long, shown in Figure 2.1. The entire T-RExE setup can include up to five cylindrical sections and two semi-spherical end caps. The cylindrical sections are S235JRG2-EN10025 hot rolled steel 1m in diameter and 10mm thick with St. 52.3N alloy steel DN1000 x 80mm flanges welded onto the lip. The sections are manufactured per DIN28032-PN16, where DN refers to the nominal internal diameter in mm, PN the pressure number rating in bar, and DIN (Deutsches Institut für Normung) the German national organization for standardization. There are two 0.25m long, one 0.4m long, and two 0.6m long cylindrical sections that are available for use.

The 0.6m long cylindrical sections, which have portholes welded onto the shell, are the only two cylindrical sections used in the experimental setup described here. The portholes are C22.8 Carbon Steel DN300-PN16 flanges welded onto 12″ diameter A106 Grade B Carbon Steel seamless pressure pipe shells. Similarly, C22.8 DN100-PN16 flanges were welded onto 4″ diameter St 35.8 pipes, and C22.8 DN50-PN16 flanges onto 2″ diameter St 35.8 pipes for the smaller portholes on the end caps. All portholes have a mating blind-flange

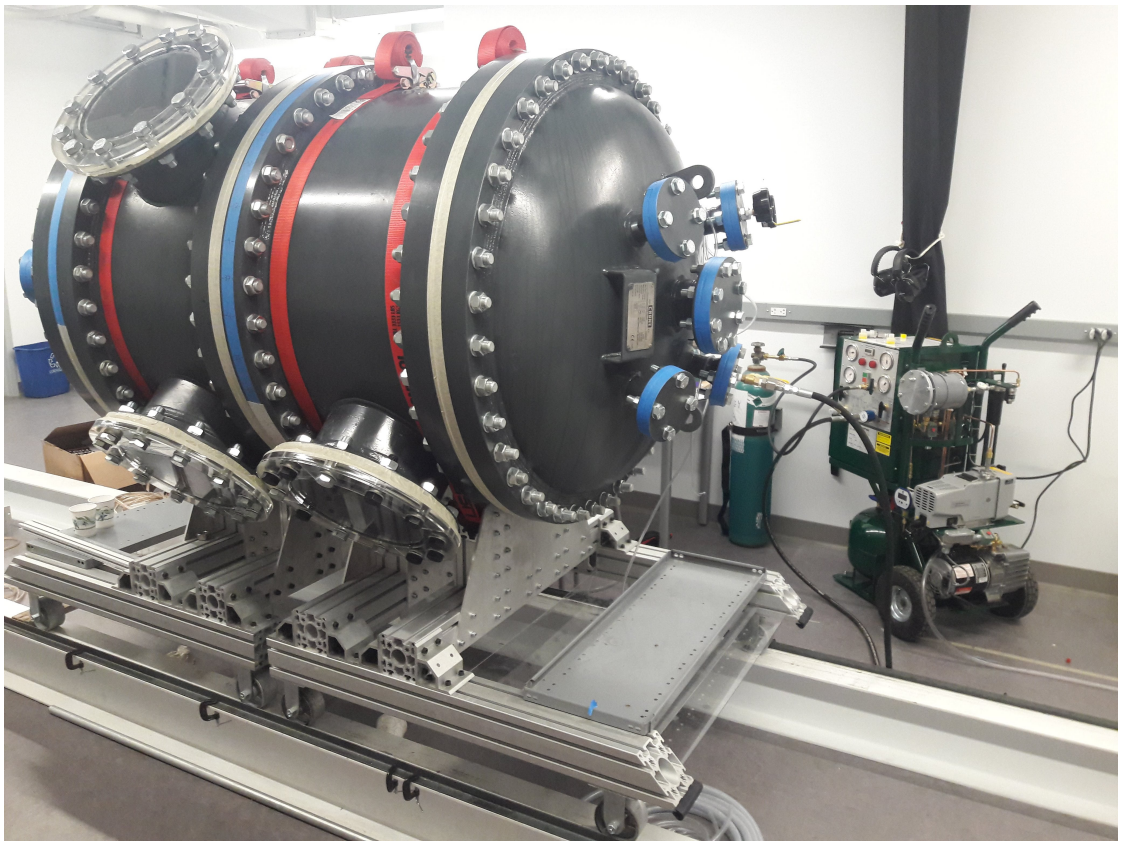

Figure 2.1: T-RExE including Pumping System

circular plate that mounts to the outside of the porthole. All surfaces, excluding mating surfaces, were coated with a rust-preventative, electrically-isolating paint.

### 2.1.1 Mounting

The two cylindrical sections were mounted onto rolling carts with portholes oriented at a $45^o$ angle, shown in Figure 2.2. This design ensured the entire weight was supported by the cylindrical shell and not by portholes or weld seams, also making all four portholes accessible in the case that camera tracking

experiments are used in future.

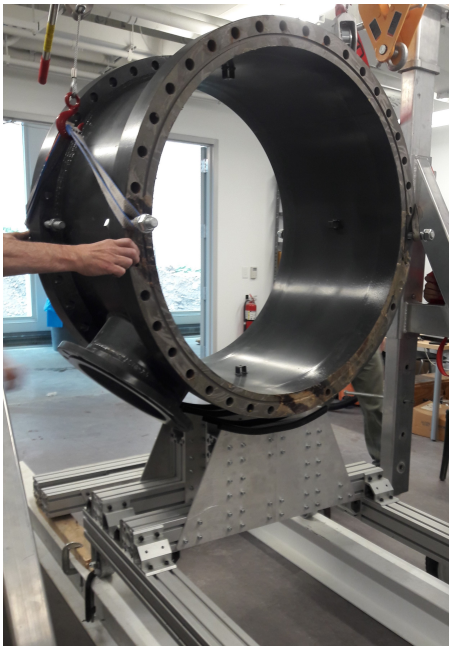

Figure 2.2: Pressure Vessel Cylindrical Section

The rolling carts, as seen in Figure 2.3, were built using water-jet cut 1/4" thick aluminum plates, Misumi aluminum 8 series 100x100mm 4-side slotted beams, and custom-made brackets from extruded aluminum corner struts. Each aluminum plate was manufactured in two pieces, due to the limited size capability of the water jet cutter at Cornell's Clark Hall Machine Shop. A 55A durometer, EPDM rubber U-channel trim, McMaster 8693K22, lines the top of the aluminum plates to provide additional support. The rubber trim not only secures the pressure vessel cylindrical section in place but also electrically isolates the pressure vessel from the metal cart.

Four semi-steel iron SCC-30R420-SSR 4" rigid Service Caster wheels, rated up to 1000 lbs, were used at the base of each cart. The wheels enabled the carts to roll the pressure vessel along the 20ft long I-beams installed in the lab. The I-beams redistributed the T-RExE's approximate 1.5 ton weight away from the

floor center to the building's structural beams. I-beams 5-1/4″ wide by 8″ tall were installed so that the beams bow upwards in the center, remaining off the unsupported, unreinforced floor section.

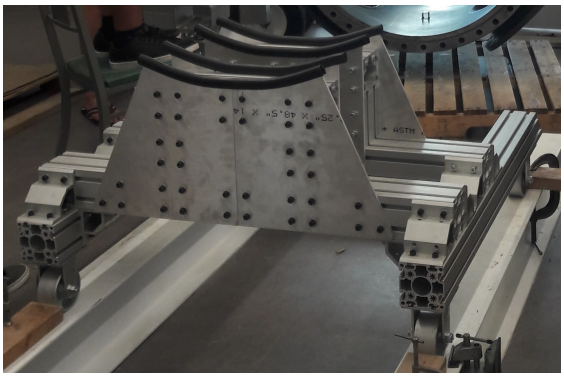

Figure 2.3: Assembled Cart

The center of mass of each pressure vessel half was barely inside the supporting water-jet aluminum plates. While various structural designs were considered for supporting the end caps, the rounded end cap shape proved difficult to reinforce. The end caps were manufactured with lifting eye nuts to support the end cap weight in tension, but not in compression as needed for these structural designs. To ensure the pressure vessel's would not tip over the aluminum plate's supporting edge during operation, two US Cargo Control 5420FE-RED 2″x20ft 10,000 lbs static load (3,000 lbs working load) ratchet straps were looped over each cylindrical section and through the supporting beams, as seen in Figure 2.4.

To keep the carts on the raised I-Beam tracks, three 1″ A36 hot rolled steel angles, Online Metals #9906, each 6ft long, were secured to each I-beam outside edge with multiple 1″ C-Clamps, Pittsburgh #37842. Thus, 18ft of the I-beam is available for the carts to separate.

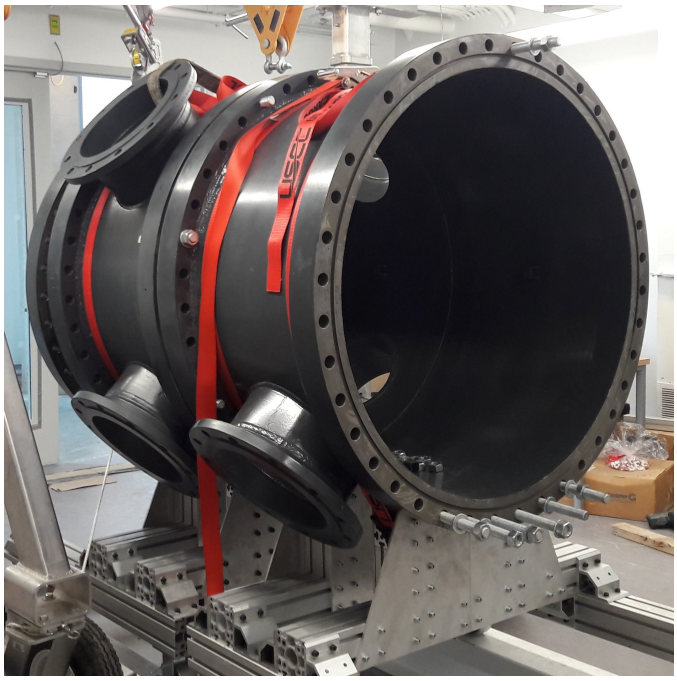

Figure 2.4: Assembled Pressure Vessel and Cart

The cylindrical sections are bolted together with forty M24 bolts. Each end cap is permanently bolted to its respective cylindrical section and the two halves bolted together periodically for experiments. The bolts are twice torqued per the standard 40-bolt torque sequence up to approximately 15 ft-lbs, then each bolt checked sequentially clockwise. However, for experiments run at low pressures, not all forty bolts need be used.

### 2.1.2 Gaskets, O-rings, and Windows

Rubber gaskets for the large and small portholes were cut from 0.062″ thick 50A durometer Neoprene rubber to the dimensional standards for soft rubber gaskets per DIN and PN specifications. The gaskets were placed onto each port-hole flange with a small layer of Super Lube Multi-Purpose Synthetic Grease to

create a pressure-tight seal.

Rubber O-rings for the cylindrical section O-ring grooves were cut to length from Global O-ring 8.40mm EPDM 70 durometer cord stock and glued at a $45^o$ angle. The O-rings were also greased with the same synthetic grease as above to provide a pressure-tight seal. All mating surfaces were sanded smooth and cleaned of potential leak-causing debris.

To enable potential PIV or particle tracking capabilities, clear plastic windows were designed and manufactured for the large portholes. Acrylic plates 1" thick were chosen for their superior optical properties as well as structural integrity against bending from differential pressure loading. Although Acrylite® cell cast sheet material has a tensile strength of 10,000 psi and compressive yield strength of 18,000 psi, the material capabilities are limited by the 1,500 psi strength against stress crazing. A brittle material crazes when small networks of very fine cracks form on the material surface after subjected to loading. To prevent crazing in acrylic plates, the maximum imposed material design load did not exceed the crazing strength.

The acrylic porthole windows were laser cut by the Digital Design and Fabrication Studio in the College of Human Ecology at Cornell University. Because each laser cut pass could only cut 0.6" deep into the acrylic, each plate was laser cut with a nontraditional second pass. The windows were manufactured to the same dimensional standards as the mating plates for DN300-PN16 flanged portholes. Per the ANSYS analysis of the final design, the porthole windows could handle up to 3.3 bar internal pressure before the material starts crazing, or up to 7 bar before yielding or cracking occurs.

The porthole flange geometry, with a raised lip just inside the bolthole pattern, resulted in unprecedented bending of the acrylic windows when the twelve M24 bolts that hold the plate in place were torqued. This deformation introduced unwanted mechanical stress within the window, and essentially transformed the window into a convex lens, which is not ideal for optical measurement techniques. An aluminum reinforcement ring-shaped plate and a thick hard rubber spacer were designed and prototyped to mitigate this issue. The ring plate transferred the bolting force through the aluminum and rubber, rather than through the fragile acrylic window, onto the raised flange. The ring plate design showed promising results in both ANSYS computational simulations as well as dimensional analyses of the installed prototype. It is recommended that each acrylic porthole be equipped with an aluminum reinforcing ring before further experimentation.

### 2.1.3 Feedthroughs and Gauges

A few select portholes had the acrylic window installed, while others the original 1" thick steel plates. Notably, the steel plate bolted to the porthole closest to the pressure transducer and power supply equipment was outfitted with several pressure-tight feedthroughs. Three 0.25" diameter conductor, 1/2" NPT Solid Sealing FA14321 feedthroughs were installed to provide power to the 3-phase fan placed inside the pressure vessel. Copper connectors were designed and machined in-house to electrically connect the copper conductors to the fan wiring. This configuration was chosen so the fan's motor controller could be placed outside the pressure vessel and monitored for overheating. An additional 1" NPT Pave 4762 feedthrough, with twelve 18 AWG conductors, was

installed to provide power to the internally mounted speakers and to measure the resistance of the US Sensor/Littelfuse Inc USP10982 thermistor for internal temperature readings.

The static and dynamic pressure ports from the Pitot tube were routed to the pressure transducer via a multi-conductor Omega Corporation MFT-18-4, 1/2″ NPT feedthrough. The feedthrough allowed up to four 1/8″ maximum OD probes to be installed, each compressed by a single-use stainless steel ferrule. Small 1/8″ OD 3003 aluminum hollow tubes, McMaster 7237K14, were used to provide access to the pressure ports. The 85A durometer, 1/8″ ID, flexible polyurethane tubing connected the Pitot pressure ports through the feedthrough and from the feedthrough to the pressure transducer.

To reduce the cross-talk between electrically noisy fan power wires and low-power hot wire signal, the hot wire signals were rerouted through another Pave 4762 feedthrough in an end cap porthole. As these channels were placed very close together, it is recommended a single channel is used at a time so the hot wire signal has a high signal-to-noise ratio. Still, multiple hot wire measurements could be taken simultaneously if desired. The spare feedthrough wires were also used to power the traverse which positionally translates the probe mount radially within the pressure vessel.

A 3/8″ NPT Apollo 94A-102-01 two-way ball valve, installed in the end cap porthole plate with an Eaton Aeroquip 2083-8-4S 3/8″ NPT adapter, controlled the gas flow between the pressure vessel and the Enervac GRU-4 $SF_6$ pumping system. The line was equipped with a DN-8 connector, a pressure-tight fitting that maintained pressure in the line when disconnected.

Two analog pressure gauges were installed in the end cap porthole plate to monitor vacuum and positive pressures. The vacuum SPAN LFS-210-(-1 Bar)-G gauge can measure from -1 to 0 bar gauge, with 10mbar degradations. The positive pressure SPAN LFS-210-(2 Bar)-G gauge can measure 0 to 2 bar gauge, with 20mbar degradations. The pressure degradations on these two instruments was sufficient for experimental purposes, so the desired experimental pressure could be reached within +/- 5 or 10 mbar respectively. A Nigo 1/4" NPT 180SS Series three way ball valve was installed to allow pressure to be measured either by the vacuum gauge or by the positive pressure gauge, as each gauge should only be subjected to pressures within the indicated pressure range. Subjecting a gauge to pressures outside their range could damage their internal sensor.

All NPT connections were installed using Teflon® tape for a pressure-tight seal.

### 2.1.4 Pressure Relief Valve

A pressure relief valve (PRV) was installed to prevent the internal pressure from rising above the acrylic window crazing strength pressure. The PRV became critical in three cases.

1. **Air Flow from the Building Air Supply**

   When gas flows from high pressure to the pressure vessel through a small orifice, the orifice acted as a converging-diverging nozzle. The flow is choked when the downstream pressure is less than a critical pressure $p^*$:

$$\frac{p^*}{p_o} = \frac{2}{\gamma + 1}^{\frac{\gamma}{\gamma - 1}}$$

where $p_o$ is the upstream stagnation pressure and $\gamma$ the ratio of specific heats. When the flow is choked, the gas reaches sonic speed at the throat and the mass flow is at a maximum. As the pressure from the building air supply is 80psi (5.5 bar), the critical pressure is 2.9 bar for the air properties in Table 2.1. Since the internal pressure will be the PRV overpressure set to the maximum allowable acrylic plate pressure 3.3 bar, the internal pressure is higher than the critical pressure and the flow is not choked. Thus, isentropic relations can be applied to determine the mass and volumetric flow rate based on the smallest orifice in the equipment line, which is 1/8" ID at the building air supply hose nozzle. The Mach number M can be calculated using the following isentropic relation:

$$M = \sqrt{\left(\left(\frac{p_o}{p}\right)^{\frac{\gamma-1}{\gamma}} - 1\right)\frac{2}{\gamma-1}}$$

where $p$ is the downstream pressure. Under these conditions, the flow at the throat is Mach 0.8. To calculate mass flow rate $\dot{m}$ the following relation is used:

$$\dot{m} = \rho A_l \bar{U} = \rho A M c$$

where $\rho$ is the density typically determined with the ideal gas law $\rho = P/RT$, $R$ is the gas constant, $T$ temperature, $A_l$ the smallest effective area in the line, and $U$ the velocity signal and $\bar{U}$ its mean. Speed of sound c is calculated as:

$$c = \sqrt{\gamma RT}$$

At these conditions, the mass flow rate is 0.0094 kg/s, and the volumetric flow rate 5.1 CFM at internal pressure p and room temperature T. To correct to standard pressure and temperature conditions:

$$SCFM = CFM\frac{p}{p_{ref}}\frac{T_{ref}}{T}$$

Table 2.1: Gas Properties

| Gas | $\mu$ [Pa-s] | $\gamma$ | c [m/s] | $\mathcal{M}$ [g/mol] | $c_p$ [J/kg-K] | $k$ [W/m-K] |
|---|---|---|---|---|---|---|
| Air | $18.49 \times 10^{-6}$ | 1.4 | 345 | 28.9 | 1005 | 0.024 |
| $SF_6$ | $15.12 \times 10^{-6}$ | 1.1 | 136 | 146.0 | 669 | 0.0136 |

where $p_{ref}$ is the reference pressure at 1 bar and $T_{ref}$ the reference temperature at $528^o$R. Correcting for standard conditions, the flow rate is 16.9 SCFM.

2. $SF_6$ **Flow from the Enervac System Storage Tank**

   In the second case, $SF_6$ gas is routed into the pressure vessel from the onboard gas tank of the $SF_6$ pumping system discussed below, which can be pressurized up to 298 psig (21.5 bar). Per the equations above and the $SF_6$ gas properties in Table 2.1, the critical pressure is 12.5 bar. Since the internal pressure is below this value, the flow is choked and the mass flow rate can be calculated as:

$$\dot{m} = C_d A_l \sqrt{\left(\gamma \rho_o p_o \frac{2}{\gamma+1}\right)^{\frac{\gamma+1}{\gamma-1}}}$$

   where $\rho_o$ is the upstream density at stagnation pressure. Using discharge coefficient $C_d = 0.7$ [23], and the area of the smallest orifice having 1/8" ID, the mass flow rate is 0.0574 kg/s, or 6.2CFM at internal pressure and room temperature, and 20.6 SCFM at standard conditions. However, this $SF_6$ SCFM flow rate needs to be corrected to be put in terms of air. A correction factor of 0.44 is calculated by extrapolating correction data in the Apollo Pressure Relief Valve selection guide manual [24]. The effective flow rate is 20.6 SCFM/0.44 = 46.9 SCFM.

3. $SF_6$ **Flow from the Auxiliary Tank**

The last case that needs examining is $SF_6$ routed from the Enervac pumping system onboard storage tank, with a maximum 69 bar storage capability. For this upstream pressure, the 40 bar critical pressure is far higher than the 3.3 bar overpressure, therefore the flow is choked and mass flow rate is 0.184 kg/s, or 20.1 CFM at internal pressure and 150 SCFM at standard pressure.

The Apollo Conbraco 19KEE PRV, capable of flow rates up to 166 SCFM, was chosen since this PRV could handle the highest volumetric flow rate (case 3 at 150 SCFM) to prevent the windows from crazing. The PRV set pressure was set at 30 psig (3 bar), at which point the PRV begins to open. The PRV is fully engaged and open at the overpressure of 33 psig (3.27 bar), which is 10% above the set pressure. At this point, the PRV will release gas from the pressure vessel at the same flow rate that gas flows into the pressure vessel. This particular PRV is stainless-steel spring operated, where the spring is set to a particular length and load to ensure the PRV operates at the appropriate pressures. The PRV was installed with a 1" NPT elbow on the back vertical plate to keep the relief valve upright and aligned with gravity. Installing the PRV at an angle not aligned with gravity induces undesired loads that cause the PRV to engage at a pressure other than the set pressure.

## 2.2 Turbulence Generators

### 2.2.1 Fan

A three-phase hobby motor Freewing 90mm 12-blade 1250kV fan was mounted onto an aluminum structure at one end of the pressure vessel. The mount ensured the fan was located concentrically with the cylindrical sections and that the fan exit plane was aligned with the cylindrical section mating surface, as seen in Figure 2.5. The three power wires for the three-phase fan are shielded with 1/2″ tinned copper metal braided sleeving Electriduct CE-COMINOD041552 to limit the electromagnetic noise permeating from the high-power wires carrying up to 100A current. The three wires terminated to the internal side of the three 100A feedthroughs described above.

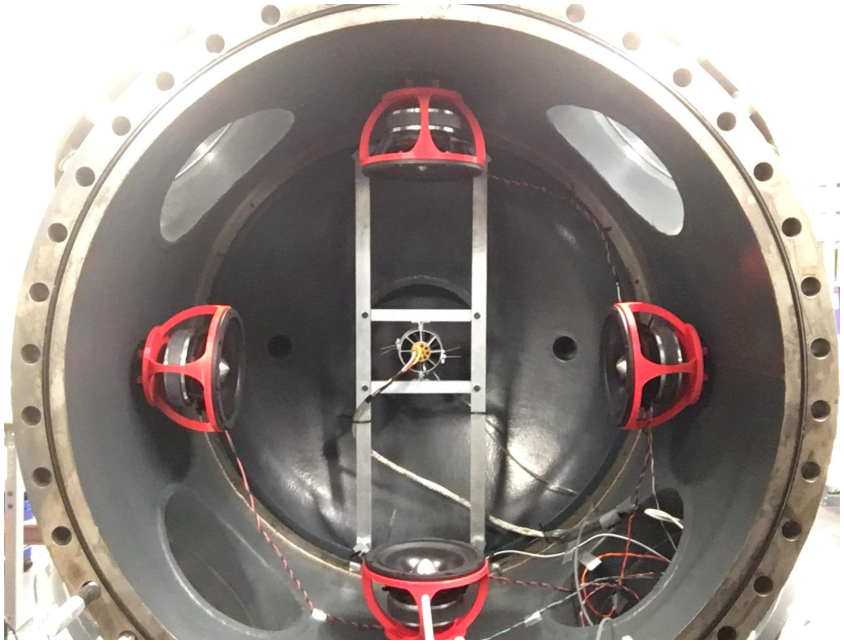

Figure 2.5: Fan and Speakers Mounted in Pressure Vessel

On the external feedthrough side, the three wires were routed through the

Castle Creations Phoenix Edge 100 motor controller, which converted a two-wire power input into the three-phase signal. The input speed to the fan was throttled by a HobbyKing LED Servo Tester, used as a speed controller in this setting. The motor controller could be powered with three 8S Traxxas Lipo batteries in series, together providing 33.3V and up to 100A. The Readytosky Lipo Battery Tester Monitor was connected with the Traxxas ID Connector Converter cable to the Lipo battery so that each cell voltage could be monitored continuously throughout experimental tests. However, running the fan at full speed drew close to 100A, so the batteries, rated for 5000mAh, could only provide enough power for 3 minutes total of data measurement. A Traxxas EZ Peak Dual Charger was used to charge the batteries in between measurement sets.

Powering the motor controller with the Volteq HY30100EX power supply, which provided up to 30V and 100A continuously, enabled data to be taken for longer periods of time. The power supply required a NEMA 10-50 electrical connection to be installed in the lab, with 110V and minimum 34A current circuit to power the device.

### 2.2.2 Speakers

The turbulent fan flow was driven past four equally spaced Cadence CVL-88MBX speakers mounted along the internal circumference of the cylindrical sections, seen in Figure 2.5. The 8" midrange speakers could provide frequencies between 60Hz and 8kHz at sound pressure levels (SPL) projected to be over 160dB. These SPL values were measured with a PCE Instruments PCE-322A Sound Pressure Level Meter with dBA filtering. The speakers were installed ax-

isymmetrically to provide equally distributed dilatational forcing on the fluid, in conjunction with the solenoidal forcing generated by the fan. The acoustic properties of the pressure vessel, which essentially acts as a resonating cavity, may potentially add to the dilatational forcing. The resonating frequency of the T-RExE was experimentally found to be 814 Hz.

The 3D-printed speaker mounts were bolted to flange tabs welded onto the cylindrical section interior surface. The speaker power was routed through the feedthrough from custom-made amplifiers as used by Bewley et al [25]. The amplifiers received the frequency signal from a standard audio jack.

The rough sketch of the general fluid flow throughout the pressure vessel is shown in Figure 2.6, where the fan (blue) created a flow past the speakers (yellow) to the hot wire probes (orange). The blue arrows indicate the fan flow directions and the yellow semicircles the speaker wave propagation. The axial (x) and radial (r) direction are also noted.

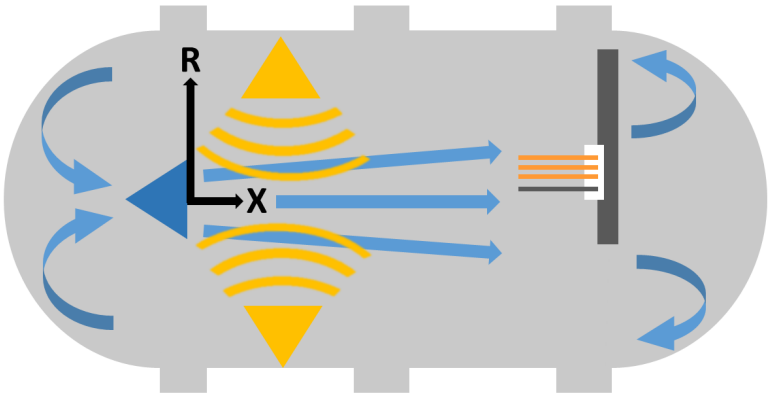


Figure 2.6: Sketch of Flow Throughout the T-RExE

## 2.3 Measurement Equipment

Opposite the fan in the pressure vessel were the measurement probes. Up to three hot wire probes and a single Pitot tube could be mounted on the probe mount, seen in Figure 2.7.

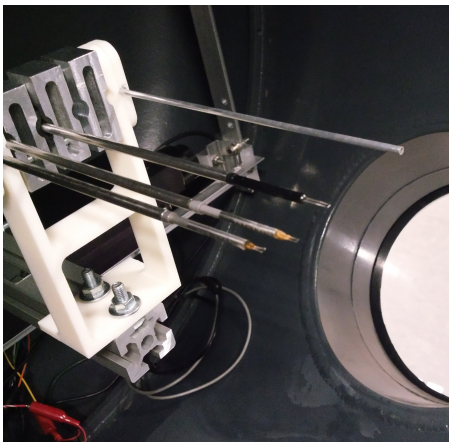

Figure 2.7: Probe Mount

### 2.3.1 Pitot Tube

The Pitot tube, a small 1/8" OD 3003 aluminum hollow tube, McMaster 7237K14, was connected to the external Validyne DP103-32 pressure transducer with 85A durometer 1/8" ID vacuum-rated flexible polyurethane tubing. The aluminum tube provided only the stagnation pressure, and the static pressure was routed from the porthole cavity near the feedthrough. In the incompressible cases, velocity is calculated using the Bernoulli equation:

$$p_o = p + \frac{1}{2}\rho \bar{U}^2$$

$$\bar{U} = \sqrt{\frac{2(p_o - p)}{\rho}}$$

In compressible cases, velocity is calculated using isentropic relations:

$$\frac{p}{p_o} = \left(1 + \frac{\gamma - 1}{2} M^2\right)^{\left(\frac{-\gamma}{\gamma - 1}\right)}$$

hence

$$\bar{U} = cM = c\sqrt{\left(\left(\frac{p}{p_o}\right)^{\frac{\gamma-1}{-\gamma}} - 1\right)\frac{2}{\gamma - 1}}$$

where the static pressure was indicated by the pressure gauge, and the stagnation pressure calculated using the static pressure and pressure transducer differential. The pressure transducer was calibrated per the Validyne manual [26], and the voltage signal read as a percent of the pressure transducer's total allowable pressure drop (2 psi for the Validyne DP103-32) using the Validyne CD23 Demodulator.

A second Pitot tube was bent into a U-shape and secured to the fan so the tube opening was flush with the fan exit plane. The pressure was routed through the pressure tube feedthrough, and the fan exit velocity calculated per the specifications above.

### 2.3.2 Hot Wire Probes

The turbulent velocity data was collected with a TSI Incorporated 1201 Platinum film probe, a traditional-sized Tungsten probe, a miniature-sized (mini) Wollaston platinum probe, and a tiny-sized Wollaston platinum probe. Table 2.2 shows the material, diameter $d_w$, length $l_w$, resistance $R_w$ and overheat ratio $a_w$ used for each probe. The traditional, mini and tiny probes were manufactured in-house using the same process used by researchers in Dr. Laurent Mydlarski's lab at McGill University. The tiny probe did not interface well with either anemome-

Table 2.2: Hot Wire Probe Properties

| Probe | Material | $d_w$ [$\mu$m] | $l_w$ [mm] | $R_w$ [$\Omega$] | $a_w$ | $a_o$ [1/C] |
|---|---|---|---|---|---|---|
| Film | Platinum | 50.80 | 1.02 | 5.7 | 1.80 | 0.0038 |
| Traditional | Tungsten | 5.00 | 1.29 | 3.5 | 1.80 | 0.0036 |
| Mini | Platinum | 1.25 | 0.30 | 20.0 | 1.30 | 0.0024 |
| Tiny | Platinum | 0.60 | 0.14 | 47.0 | 1.25 | 0.0016 |

ter, as the velocity fluctuations caused the highly sensitive and thin sensing element to quickly become unstable. NSTAPs were also attempted to be used for measurements but similarly became unstable. These smaller probes picked up more velocity fluctuations in the flow at frequencies higher than the anemometers' response frequencies. While attempting to respond quickly with the flow, the anemometers sent high currents belatedly through the sensing element to keep the temperature constant, which overheated the wire and caused the sensing element to fracture.

Each hot wire signal wire pair was shielded with 1/2" tinned copper metal braided sleeving Electriduct CECOMINOD041552 and grounded to the pressure vessel to reduce the electrical noise that contaminated the signal. The shielding acted as an electrically conductive casing that absorbed and reflected stray electromagnetic radiation from noisy signals within the lab or pressure vessel, protecting the delicate hot wire signal within. The pressure vessel, in turn, was grounded to earth ground.

### 2.3.3 Hot Wire Anemometers

The first anemometer used was the 55M01 Dantec Anemometer module, hereafter referred to as the DISA. The DISA included the 55M10 Constant Temperature Anemometer (CTA) module with a 1:20 bridge ratio, and a 55M05 power pack unit that transformed AC wall voltage into a DC voltage source. The DISA could test hot wires with a 0.3, 3 or 30 kHz square wave, and output a voltage signal at +/- 1, 3, 10, or 30 volts. A potentiometer in the wheatstone bridge circuit could be adjusted to compensate for the cable's resistance. A short-circuit wire, which is a probe with its tips soldered together so the only measured resistance is that of the probe's leads, was connected to the DISA and the zero resistance potentiometer knob adjusted. Thus, when the actual probe was connected to the DISA, the only resistance the DISA measured was the probe's sensing element resistance. The overheat resistance was set by the decade resistance knobs according to the desired overheat ratio. The DISA's maximum overheat resistance of $99.99\Omega$ limited its operation to hot wire probes with overheat resistance less than that. Thus, probes with a high resistance, such as nontraditionally small probes or NSTAPs, could not be used with the DISA. Additionally, switching operational modes sent a current spike, sometimes more than 1mA, through the connected probe, which broke the smaller diameter sensors.

The second anemometer used was the Dantec StreamLine Probe CTA system, hereafter referred to as the StreamLine. The StreamLine interfaced with Dantec's StreamWare Pro software, which calculated and optimized the Wheatstone bridge based on the resistances of the probe, probe leads, probe support and cable. The traditional probe was operated using the StreamLine's 1:20 bridge, which auto-calculated and adjusted the overheat resistance. The smaller

probes were operated using the 1:1 bridge, which used an external Bourns 3683S-1-102L click-potentiometer to adjust the overheat. Although the StreamLine was equipped with a signal filter and data acquisition system (DAQ), an external signal filter and DAQ were used for consistency between the DISA and StreamLine anemometer measurements.

### 2.3.4 Signal Filter and DAQ

The hot wire signal was filtered by the Krohn-Hite 3384 Filter, capable of filtering anywhere between 0.1Hz and 200kHz. The signal was first low pass filtered at 200kHz with a Butterworth filter, and then amplified with an appropriate gain to maximize the signal amplitude. The filtered signal was collected by the MC Measurement Computing USB-1608GX-2AO DAQ, which could sample up to 500 kHz. To avoid aliasing, the data was low pass filtered at 200kHz Nyquist frequency and collected at 400kHz. The DAQ had an analog input voltage range of +/- 10V with 16-bit resolution, and could acquire up to 8 differentially ended signals. Although the DAQ had multiplexed sampling, this was irrelevant as only one channel was used at a time for this experiment and thus the maximum DAQ sampling frequency used. The DAQ connected to the computer via USB, and the data monitored on a custom-made LabView Virtual Instrument (VI).

### 2.3.5 Probe Traverse

The probe mount was secured to an Instrument Industries PSI 103 Model traverse that varied the hot wire and Pitot tube radial position relative to the fan

flow. The traverse power and signal wires were routed through a feedthrough and connected to the controller box. To move the probe mount axially, an additional 8020 section of specified length needed to be installed on top of the traverse. The probe mount structure sat at the end of the far cylindrical section in the pressure vessel.

## 2.4 Pressurizing the Pressure Vessel with $SF_6$

The Enervac GRU-4 $SF_6$ Gas Recovery Unit provided all the pumping functions needed to evacuate air and pressurize the T-RExE with $SF_6$. Throughout this process, the pressure vessel also underwent a variety of leak tests, all outlined below. The leak rate $q$ [mbar L/s] is determined using:

$$q = \frac{\Delta(pV)}{\Delta t}$$

where $V$ is volume, which can be assumed constant over time $\Delta V = 0$, and time $t$.

1. **Pressurize Step: Overpressure with Air**

   With all openings bolted closed, the pressure vessel was pressurized to about 1.2 bar with air from the building air supply.

2. **Leak Test: Bubble Test**

   A generic brand liquid dish soap and water mixture solution was slowly sprayed onto all potential leak locations, including mating surfaces with gaskets and O-rings, Teflon® taped NPT connections, etc. If a leak was present, bubbles would begin to form. This test caught leaks on the order

of $1 \times 10^{-1}$ mbar L/s [27]. If no bubbles formed, the equipment passed this leak test.

3. **Leak Test: Air Overpressure Test**

   With the pressure vessel overpressurized as indicated above, the initial and final pressures were noted over a 24 hour period. While this test detected leaks on the order of $1.6 \times 10^{-1}$ mbar L/s, this test caught leaks at overlooked locations. If the pressure did not change within the time period, the equipment passed this leak test.

4. **Pressurize Step: Evacuate the Air**

   The GRU-4 included a Just Better Industries Air Vacuum Pump which was capable of evacuating the air out of the equipment to a 25 micron (0.035 mbar) vacuum pressure. The vacuum pump's air pump down time, seen in Figure 2.8, took one hour to evacuate the initial 90% of the pressure and 15+ hours for the residual 10%. This was typical of vacuum pump performance as the pump had to work harder to pump out the remaining air in the vessel [28]. The end pressure corresponded to 0.05kg residual air left in the pressure vessel, an amount which was deemed small enough to not noticeably contaminate the ∼9kg of $SF_6$ added in the following $SF_6$ overpressure step.

   One major issue that dramatically increased air pump down time was relative humidity, as the system had to vaporize not only water vapor in air but also the water vapor absorbed into the pressure vessel walls. Possible options to mitigate this issue in future include keeping the pressure vessel sealed closed when not in use, keeping the pressure vessel at vacuum, using a heater to evaporate the water out of the air and pressure vessel walls, or decreasing the wall surface roughness so less water is ab-

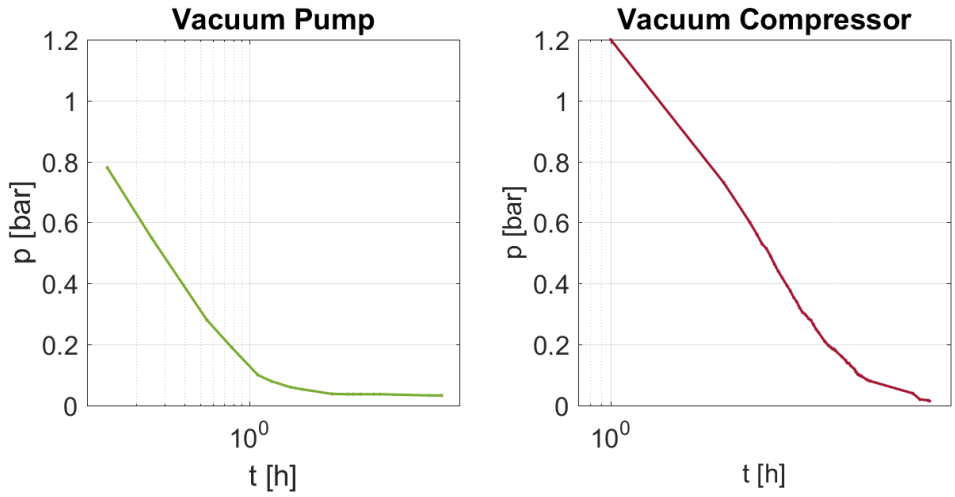


Figure 2.8: Vacuum Pump Air Pump Down, Vacuum Compressor $SF_6$ Pump Down

sorbed [29].

5. **Leak Test: Air Evacuation Test**

   This test was the same as the Air Overpressure Test, but performed again at this step in the process.

6. **Pressurize Step: Overpressure with** $SF_6$

   The pressure vessel was pumped up with $SF_6$ to about 1.2 bar by the GRU-4 compressor, the rate of which can be seen in Figure 2.9. Either an auxiliary tank or onboard storage tank supplied the $SF_6$. Overpressurizing the pressure vessel diluted the small amount of air left in the pressure vessel from the air evacuation step, ensuring the bulk of the gas remaining was primarily $SF_6$.

7. **Leak Test:** $SF_6$ **Overpressure Test**

   This test was the same as the Air Overpressure Test, but performed again at this step in the process. The $SF_6$ leak rate is typically normalized in

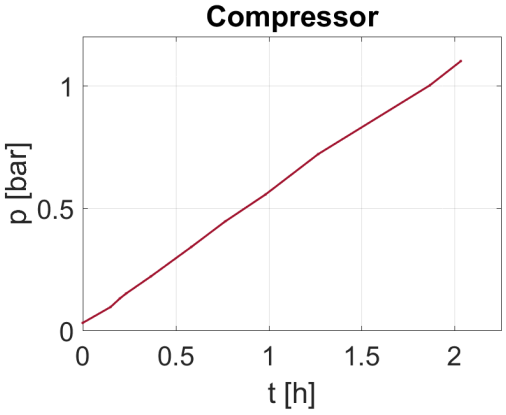


Figure 2.9: Compressor $SF_6$ Pump Up

terms of air using:

$$q_a = q_s \frac{\sqrt{\mathcal{M}_s}}{\sqrt{\mathcal{M}_a}}$$

where $\mathcal{M}$ was the molar mass, and the subscripts 'a' and 's' were air and $SF_6$ respectively. While this test detected leaks only down to $3 \times 10^{-1}$ mbar L/s, it was an integral test in determining if the pumping process introduced any leaks in the system.

8. **Leak Test: $SF_6$ Sniffer Test**

   The $SF_6$ sniffer CPS Products CPSLS790B Refrigerant Leak Detector was used to check all the leak-potential locations mentioned above. Per the detector manual [30], the detector was swept at 1 in/s and less than 1/4" away from the surface at the highest sensitivity. The sniffer could detect leaks down to $10^{-6}$ mbar L/s [27]. The O-ring-sealed cylindrical sections and gasket-sealed portholes could be taped over, which routes any leaking $SF_6$ toward the ground, as $SF_6$ is heavier than air. A small gap in the tape near the ground was left for the sniffer to test for $SF_6$.

9. **Pressurize Step: Pressurize to Experimental $SF_6$ Test Pressure**

   Once it was confirmed the equipment was leak-tight, the pressure vessel

was pumped to the desired $SF_6$ pressure for experiments.

10. **Pressurize Step: Evacuate the $SF_6$**

    Because $SF_6$ is a potent greenhouse gas [31], an Agilent Dry Scroll Vacuum Compressor Pump was added to the original GRU-4 unit to reduce the amount of $SF_6$ released into the atmosphere after each experiment. This additional vacuum pump could reduce the $SF_6$ pressure to 1 mbar, compared to the typical 5 mbar of most other pumping systems. Thus only 0.009kg of $SF_6$ was released into the atmosphere each experimental cycle rather than five times that amount. The vacuum compressor pump down rate can be seen in Figure 2.8.

## 2.5 Calibration

An initial calibration for each hot wire probe was performed outside the pressure vessel using a pressurized air tank connected to the building air supply. The probe was subjected to a range of velocities at the jet orifice exit, and the voltage recorded for each corresponding velocity. The calibration data taken with the DISA against the pressurized air tank is plotted with 'x' markers in Figure 2.10 for the film probe, traditional probe, and mini probe. The same is done for StreamLine calibration data in Figure 2.11, with the addition of the tiny probe.

Calibrating the hot wire probe in the fan flow first required data to be taken with the Pitot tube, then the hot wire probe at the same location, similar to Bodenschatz et al [22] and Mi et al [32]. With the Pitot tube positioned at a particular measurement location in the flow, the fan was subjected to a variety of

power settings and the Pitot tube velocity, calculated per Section 2.3.1, recorded at each power setting. The traverse was then activated and moved radially so the desired hot wire probe was placed in the same measurement location. The fan was subjected to the same power settings and the hot wire probe voltages recorded at each corresponding velocity. The data is plotted with 'o' markers in Figures 2.10 and 2.11 for both air (green) and $SF_6$ (red).

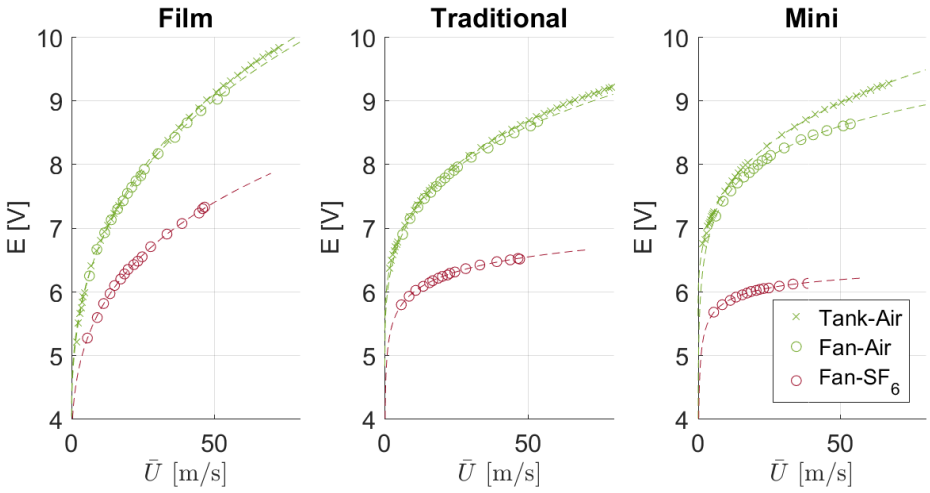


Figure 2.10: Probe Calibration with the DISA

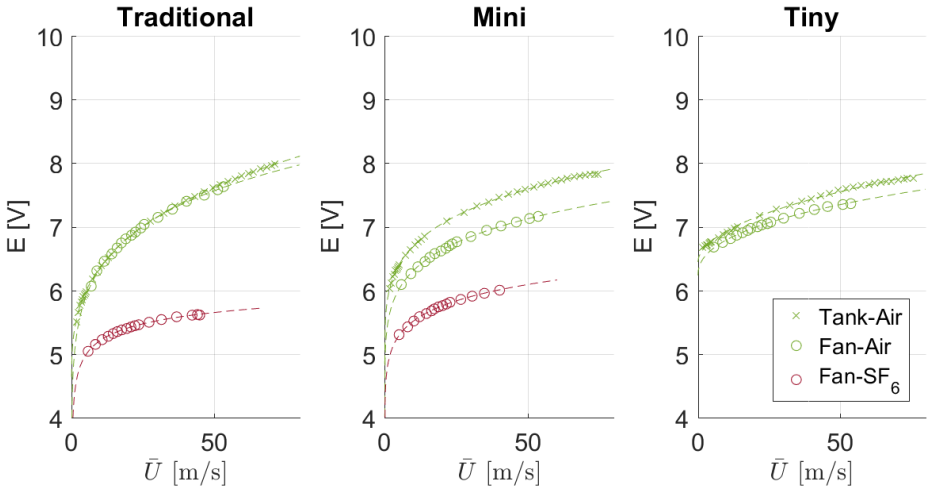


Figure 2.11: Probe Calibration with the StreamLine

The data was fit with a King's Law relation:

$$E^2 = A + B\bar{U}^n$$

with hot wire voltage $E$, and constants $A$, $B$ and $n$, plotted with a dashed line. The pressurized tank nozzle was shaped to have a sharp contraction, so the exiting velocity exhibited a top-hat profile with less than 0.2% turbulence intensity. Thus the velocity average was not skewed inappropriately by the nonlinear velocity-voltage relation.

Although the voltage magnitude depended on the filter amplifier gain, the film probe had larger voltage differences between low and high speeds because of the high overheat used. The traditional and mini probes had smaller voltage magnitudes because a lower overheat was used, despite a higher gain on the signal. The smaller probes' overheat ratios were determined experimentally to find the maximum allowable overheat that does not break the sensing element or make the probe unstable. It was desirable to use the highest overheat possible as a higher overheat increases the frequency response and sensitivity of the probe [33].

For the DISA anemometer data seen in Figure 2.10, there was relatively good agreement between the pressurized tank and in-situ fan calibration curves for the film probe and traditional probe. However, significant drift can be seen for the mini probe calibrations due to the small diameter sensing element. In order to maintain constant temperature, the anemometer sent a higher current through the probe when the probe was subjected to higher velocities. The higher current could heat up the wire, causing the material to anneal and the sensing element to change resistance.

The mini probe was subjected to an annealing period before use where it

was operated for 24+ hours with a higher overheat and no mean flow, as was similarly done for NSTAPs [34]. The mini probe in particular needed to be monitored for these changes between measurements and constantly re-calibrated to account for drift. Similar phenomena can be seen for the StreamLine anemometer data seen in Figure 2.11, with the tiny probe also exhibiting significant drift. Still, both the mini and tiny probes maintained a continuous relation despite the drifting calibration curve.

The response frequency and sensitivity of the hot wire probes were heavily reliant on the heat transfer rate from the overheated hot wire probe to the fluid. The convective heat transfer over a cylinder could be determined from the Churchill-Bernstein relation for the Nusselt Number $Nu$:

$$Nu = 0.3 + \frac{0.62Re^{1/2}Pr^{1/3}}{(1+(0.4Pr)^{2/3})^{1/4}}\left(1+\left(\frac{Re}{282,000}\right)^{5/8}\right)^{4/5}$$

$$Pr = \frac{c_p\mu}{k}$$

with $Pr$ Prandtl Number, $c_p$ specific heat for constant pressure, $\mu$ dynamic viscosity, and $k$ thermal conductivity. The Nusselt Number was also defined as:

$$Nu = \frac{hd_w}{k}$$

with heat transfer coefficient $h$, which contributed to the heat transfer rate $Q$:

$$Q = h(\pi d_w l_w)(T_w - T_o)$$

with the wire temperature $T_w$ and ambient temperature $T_o$. The wire temperature was calculated using:

$$T_w = \frac{a_w}{a_o} + To$$

with $a_o$ the material coefficient of resistance. Using the gas properties per Table 2.1 and material properties per Table 2.2, the $SF_6$ heat transfer rate was approximately 50% of that for air, which was why the $SF_6$ calibration curve was shifted

far below the air case. Therefore, since more heat was transferred in the air case, the hot wire was more sensitive to the velocity fluctuations in air than in $SF_6$.

CHAPTER 3

# LARGE SCALE FLOW CHARACTERISTICS

The following sections describe large scale flow characteristics within the T-RExE.

## 3.1 Air and $SF_6$ Experimental Pressure Settings

The $SF_6$ pressure was selected so that the gas achieved the same Taylor Reynolds Number $Re_\lambda$ as air at standard temperature and pressure, but reached a different turbulent Mach Number $M_t$:

$$M_t = \frac{u'}{c}$$

$$Re_\lambda = \frac{u'\lambda}{\nu}$$

where $u'$ was the 3D rms of the fluctuating velocity $u$, $\nu$ was kinematic viscosity, and $\lambda$ was the Taylor scale:

$$\lambda = \sqrt{\frac{15\nu}{\varepsilon}}u'$$

The Taylor scale depended on dissipation $\varepsilon$, which quantified the rate at which energy of the large scale was lost to smaller scales. The dissipation approximation used here was defined as:

$$\varepsilon = C_\varepsilon \frac{u'^3}{l_o}$$

with $l_o$ as the integral length scale, and coefficient $C_\varepsilon \sim 1$ [35]. To match Reynolds Number:

$$Re_{\lambda a} = Re_{\lambda s}$$

$$\frac{u'_a \lambda_a}{\nu_a} = \frac{u'_s \lambda_s}{\nu_s}$$

Assuming $u'_a = u'_s$ and $\lambda_a = \lambda_s$ given the same fan speed conditions, later proven in Section 3.2:

$$\nu_a = \nu_s$$

$$\frac{\mu_a}{\rho_a} = \frac{\mu_s}{\rho_s}$$

where $\mu$ was assumed to be relatively constant within the range of pressures used here. Combined with the ideal gas law $p = \rho RT$, the equation became:

$$\frac{\mu_a}{\frac{p_a}{R_a T}} = \frac{\mu_s}{\frac{p_s}{R_s T}}$$

Assuming temperature was constant $T_a = T_s$, the $SF_6$ experimental pressure should be set to:

$$p_s = \frac{\mu_s R_s}{\mu_a R_a} p_a$$

which for $p_a = 1.0$bar evaluated to $p_s = 0.16$ bar using the gas properties from Table 2.1. The remaining sections in Chapter 3 show this $SF_6$ experimental pressure preserved the large scale flow structures seen in air at atmospheric pressure.

## 3.2 Fan Characteristics

### 3.2.1 Power Profiles

Each fan power input setting $P_f$ produced a singular fan exit velocity value $\bar{U_f}$, as measured by the Pitot tube positioned at the fan exit plane. The velocities were calculated according to the incompressible and compressible conditions per Section 2.3.1. Figure 3.1 shows $\bar{U_f}$ for air (green) coincides well with that for

$SF_6$ (dark red) for various power settings. The Reynolds Number based on the fan diameter D is:

$$Re_D = \frac{\bar{U_f} D}{\nu}$$

which also matches for the two cases.

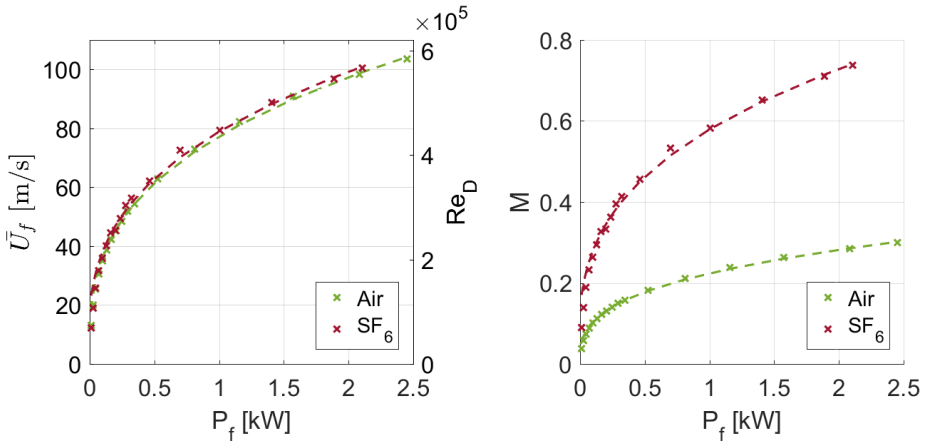


Figure 3.1: Velocity, Reynolds Number and Mach Number Power Profiles

The relation between power and velocity can be found by starting with the incompressible Bernoulli equation:

$$p_1 + \frac{1}{2}\rho \bar{U_1}^2 + \rho g z_1 = p_2 + \frac{1}{2}\rho \bar{U_2}^2 + \rho g z_2$$

where $z$ is height. Point 1 is chosen to be far upstream of the fan such that $\bar{U_1} = 0$, and point 2 immediately upstream of the fan such that $\bar{U_2} = \bar{U_f}$. As both points are along the same horizontal plane, $z_1 = z_2$, and $\rho$ is constant, the revised Bernoulli equation is:

$$p_1 - p_2 = dp = \frac{1}{2}\rho \bar{U_f}^2$$

Assuming power is proportional to force F:

$$P_f = F\bar{U}$$

and force related to change in pressure for an area:

$$F = dpA_f$$

the equation evaluates to:

$$P_f = \frac{1}{2}\rho \bar{U_f}^3 A_f$$

or more generally:

$$P_f = C_f \bar{U_f}^3$$

This relation matched that from Bodenschatz et al [22]. Coefficient $C_f = \frac{1}{2}\rho A_f$ was explicitly calculated to be $2.99 \times 10^{-3}$ for air and $2.45 \times 10^{-3}$ for $SF_6$. The coefficient derived from the curve-fit experimental power-velocity data was $2.17 \times 10^{-3}$ for air and $2.06 \times 10^{-3}$ for $SF_6$, plotted as a dashed line in Figure 3.1. These derived values deviated 27% and 15% for air and $SF_6$ respectively, errors which might be due to violations of the inviscid assumption.

Figure 3.1 also shows the relation between power and Mach Number, where $M_s \sim 2.5 M_a$ due to the smaller speed of sound in $SF_6$. For any input power setting, $Re_D$ and $\bar{U_f}$ remained constant for both gases while $M$ is much higher for $SF_6$. With the fan operating at its highest power to produce $M \sim 0.75$ in $SF_6$ at the fan exit, the tips of the fan blades were actually rotating with absolute speeds $M \sim 2$.

### 3.2.2 Axial Profiles

The axial profiles in air were mapped using the film probe, chosen primarily for its small drift but also for its high degree of spatial filtering. When the sensing element length is larger than the smallest length present in the flow, the sensing

element does not accurately measure all of the length scales and instead spatially averages these scales. This is desirable when measuring mean flow, and disadvantageous when resolving small scales. Figure 3.2 shows the mean velocity along the fan axis $\bar{U}_0$ generally decays with axial distance, where the top x-axis shows $x/D$ and the bottom x-axis $x/L$. Length $L$ was the distance between the fan exit plane and probe mount structure, $L = 1.2$m. Since $0.1 < M < 0.15$ for the air axial profile, $M$ was well within the incompressible range $M < 0.3$.

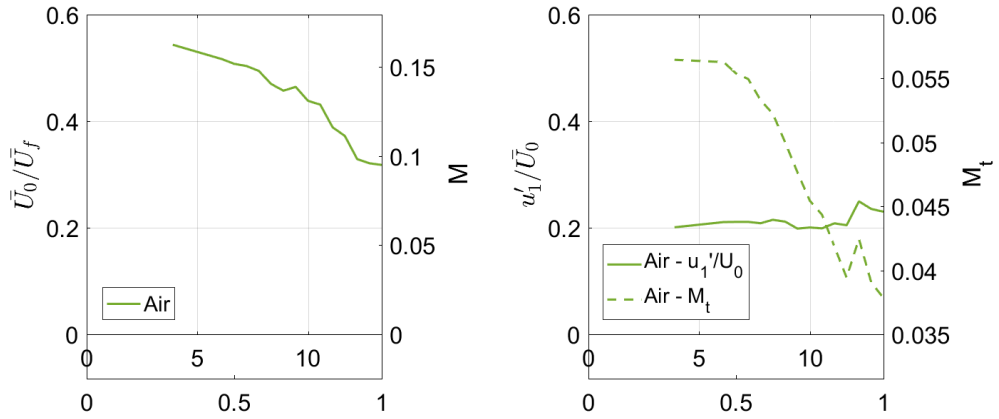


Figure 3.2: Velocity, Mach Number and Turbulence Intensity Axial Profiles

The turbulence intensity axial profile is shown by the solid line in Figure 3.2, where $u_1'$ is rms of 1D fluctuating velocity $u_1$. Turbulence intensity is fluctuating velocity rms divided by the mean. The turbulence intensity hovered around 0.2, which was predicted by Pope and Antonia for turbulent jet flow [36, 37]. There is a pronounced spike at the probe mount structure $x/L > 0.9$. At this point $\bar{U}_0$ remained steady but the turbulence intensity increased, indicating the probe mount structure obstructed the flow and introduced velocity fluctuations. The turbulent Mach Number, dashed line in Figure 3.2, followed a continuously decreasing trend with axial distance, with the flow obstruction from the probe mount structure seen in the distinct peak for $x/L > 0.9$.

### 3.2.3 Hot Wire Probe Position

Although the objective of this work was to study high $M_t$ flows, measuring the flow close to the fan exit, where $M$ and $M_t$ are maximum, could reveal structures from the rotating fan blades rather than from the developed turbulence. If the hot wire probe was set to measure farther downstream, the flow would have more time to mix and become homogeneous, isotropic turbulence. Because turbulence of this nature is invariant to reflections and rotations, a single sensor hot wire probe could reveal more information about the entire three-dimensional structure of the flow. Typically, the turbulence far downstream along the jet centerline approaches isotropy [38]. If homogeneity and isotropy are assumed, the rms of the 1D and 3D velocity fluctuations are related as $u' = \sqrt{3}u'_1$.

Mean and fluctuating velocity decreased radially outward, where the anisotropic shear stress became more prominent. Spatial filtering was more prevalent with a higher shear rate, which negatively impacted the small scale isotropy [39]. Since $\bar{U}$ and $u'_1$ were highest and shear stress minimal on the fan axis, the measurement location was chosen to be at $x/L = 0.66$ ($x/D = 8.8$) and $r/D = 0$.

### 3.2.4 Radial Profiles

Radial profiles of the mean velocity for air and $SF_6$ at $x/D = 8.8$ were also mapped with the film probe for consistency, seen in Figure 3.3. For the velocity vs $r/D$ plot, the $SF_6$ profile had a sharper decline in velocity near the fan axis compared to air with a larger jet width, perhaps from slight mismatches in kinematic viscosity. The profiles collapsed when plotted against the jet half-width

$r_{1/2}$, which describes what radial position in the flow has 50% of the fan axis mean velocity:

$$\bar{U}(x, r_{1/2}(x)) = \frac{\bar{U}_0(x)}{2}$$

The profiles remained consistent for $x/D < 12$, despite this trend typically only being valid for $x/D > 30$ [36]. At $x/D < 13$, the flow profile development was inhibited by the probe mount structure, which accounts for the deviation from the collapse at this axial distance downstream.

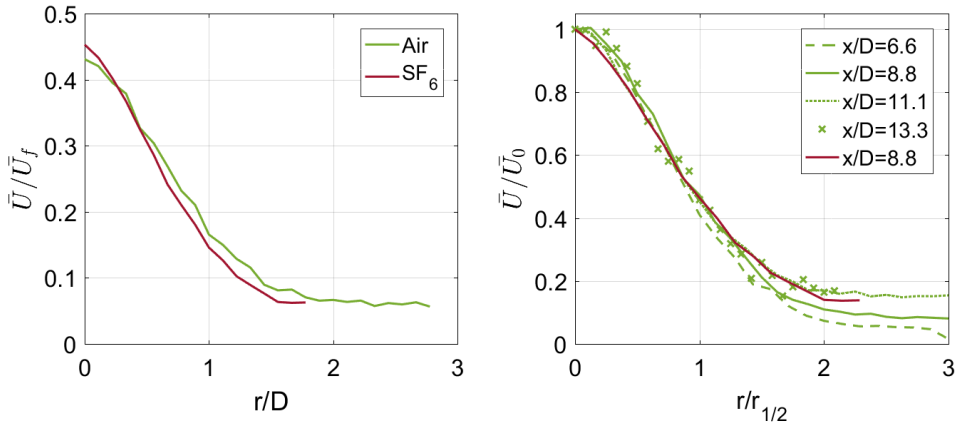


Figure 3.3: Mean Velocity Radial Profiles

Figure 3.4 shows the turbulence intensity radial profile for $x/D = 8.8$. For both air and $SF_6$, the turbulence intensity grew from 0.2 on the fan axis and increased radially outward [36]. Theoretically, the turbulence intensity could grow without bound as $\bar{U}$ approaches zero.

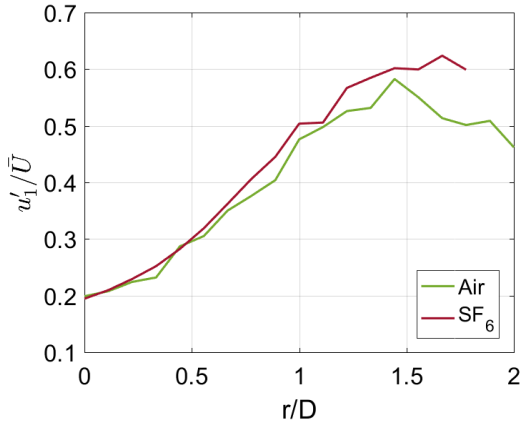


Figure 3.4: Turbulence Intensity Radial Profiles

### 3.2.5 Integral Length Scales

The 1D x-direction integral scale was calculated by integrating the correlation function and normalizing by the velocity fluctuations:

$$l_o = \frac{1}{u_1'^2} \int_0^\infty \langle u_1(x + r_x) u_1(x) \rangle dr_x$$

where $r_x$ indicates the incremental $x$ distance along the hot wire velocity signal [22]. For all fan velocities, the integral scale at the hot wire flow position was calculated to be 0.054m in air and 0.056m in $SF_6$. Since the integral length scale varied between gases by $< 3\%$, the remaining analysis uses the average 0.055m, which is remarkably close to the fan radius of 0.045m. Since the experimental setup remains the same for all speeds and gases, the same fan length scale drove the large scale flow and was found in the turbulence as the integral length scale, regardless of experimental flow conditions.

## 3.3 Speaker Characteristics

High SPL speakers were used to generate dilatational motion in the solenoidal fan turbulence. Figure 3.5 shows a logarithmic correlation between SPL and speaker input power $P_{sp}$ in air, where SPL magnitude differed based on speaker frequency $f$. The SPL spiked at high power for 111Hz and 202Hz because the speakers are over-powered to the point that the speaker cone physically impacts its frame. This impact added a second source of noise that is not at the speaker input frequency.

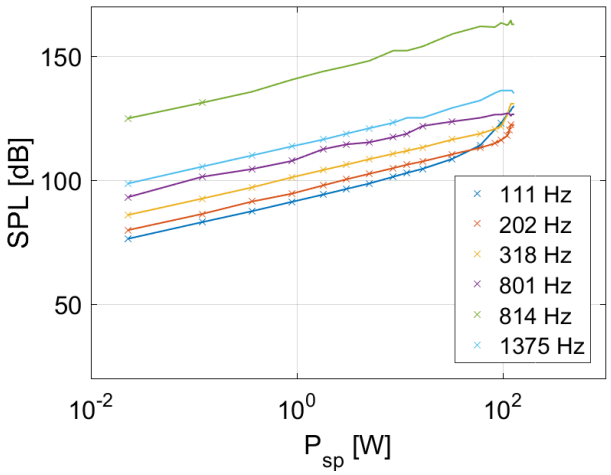


Figure 3.5: SPL Power Profile

The frequency sweep test in Figure 3.6 demonstrates the SPL sensitivity to frequency within the pressure vessel. The figure inset shows a generally higher SPL region occurring near 1kHz, with a local peak at 814Hz noted to be a T-RExE resonant frequency. Changes to the experimental setup could potentially change these resonant frequencies, as resonant modes are dependent on the entire T-RExE setup.

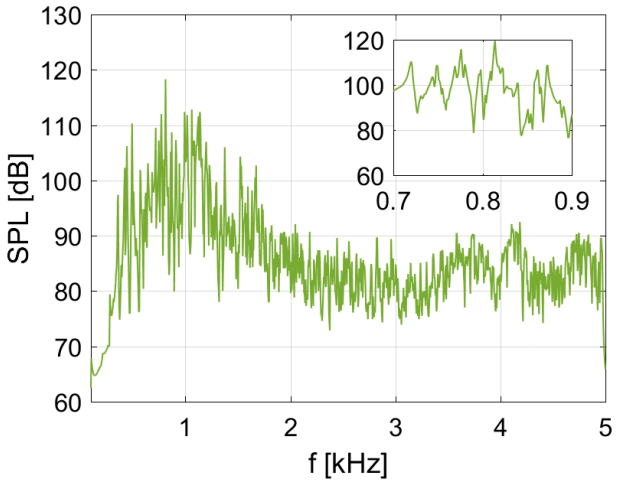


Figure 3.6: Frequency Profile

### 3.3.1 Forcing Frequencies

The speaker forcing frequencies used in experimental tests were set to particular frequencies found in the flow. In this way, the dilatational fluid motion generated by the speakers might interact with the predominant scales already present in the solenoidal fan turbulence. These frequencies were based on matching length scales or matching time scales, Table 3.1.

1. **Matching Time Scales**

   The speaker frequency $f$ corresponded to the frequency based on the eddy turnover time $\tau = l_o/u_1'$:

   $$f = 1/\tau$$

   In both air and $SF_6$, the calculated frequencies $f_{calc}$ based on the slow, moderate and fast velocity fluctuations $u'$ were given in Table 3.1. The $f_{SPL}$ values were local peak SPL frequencies found close $f_{calc}$. These $f_{SPL}$ values were chosen for testing in order to take advantage of the experi-

Table 3.1: Speaker Forcing Frequencies

| Matching Time Scales | | | |
|---|---|---|---|
| $u'$ [m/s] | $f_{calc}$ [Hz] | $f_{SPL}$ [Hz] | SPL [dB] |
| 5 | 100 | 111 | 104 |
| 10 | 200 | 202 | 116 |
| 15 | 300 | 318 | 122 |
| Matching Length Scales | | | |
| $l_o$ [m] | $f_{calc}$ [Hz] | $f_{SPL}$ [Hz] | SPL [dB] |
| .055 | 6860 | 6860 | 164 |
| .055 | 2720 | 2704 | 110 |

ment's geometry and produced the highest SPL possible, thereby inducing the largest amount of dilatation motion. The SPL column denotes the SPL used in the following experiments.

2. **Matching Length Scales**

   The integral length scale was matched to the speaker frequency wavelength $\lambda_{sp} = l_o$:

   $$f = c/\lambda_{sp}$$

   The frequencies differed based on the speed of sound in either air or $SF_6$. The $f_{SPL}$ values were chosen similarly as above.

CHAPTER 4

# SMALL SCALE FLOW CHARACTERISTICS

## 4.1 Fan Taylor Length Scales

The Taylor scale estimates at the hot wire flow position versus the associated turbulent velocity fluctuation can be seen in Figure 4.1 for the film, traditional, and mini probes. The 95% confidence interval of the true value, based on Student's t-distribution, at each setting has smaller error bars with increasing $u'$. The Student's t-distribution was chosen here since the number of samples $N$ at each setting was below thirty. The error bars are calculated using:

$$\lambda = \bar{\lambda} \pm t_{.95} \frac{\sigma}{\sqrt{N}}$$

where $t_{.95}$ is the two-tailed t-value for a 95% confidence interval based on the degrees of freedom $N - 1$. The mini probe's 95% confidence interval was generally larger than that for the the traditional probe because the smaller probe resolved higher velocity fluctuations at smaller scales.

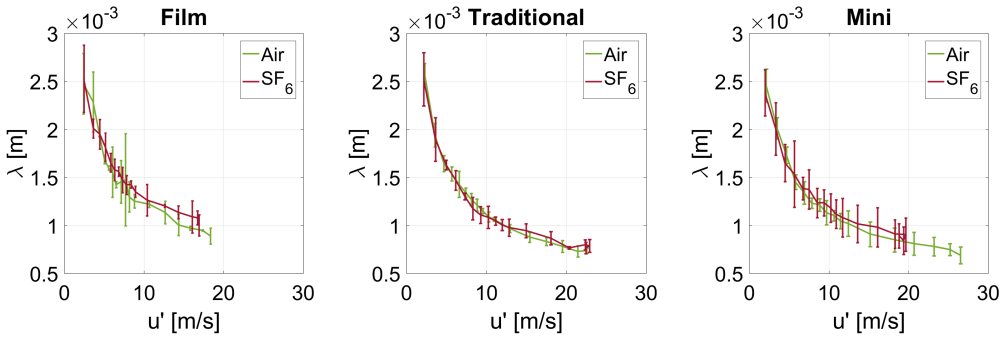


Figure 4.1: Taylor Scale Estimates

Since the Taylor scale $\lambda \sim f(u', l_o)$, the resulting Reynolds Number $Re_\lambda \sim f(u', \lambda)$ was consistent between gases since $u'$ and $l_o$ were the same. The Taylor

scale was used to calculate $Re_\lambda$, and is plotted against $M_t$ in Figure 4.2, which shows that for the same $Re_\lambda$ there are two different $M_t$ values.

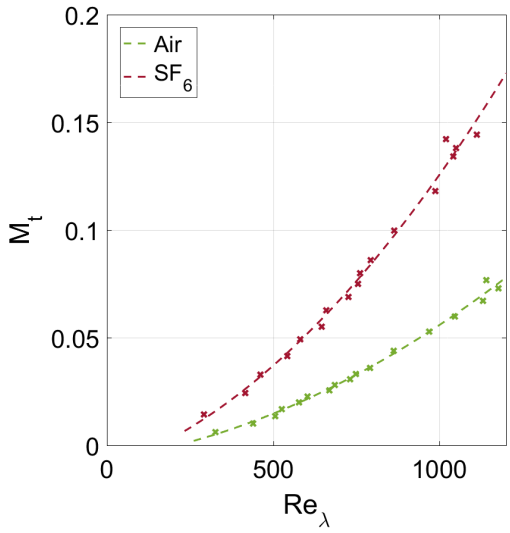


Figure 4.2: Turbulent Mach Number for Varying Reynolds Number

## 4.2 Energy Spectra

The following sections detail the energy spectra calculated at the hot wire flow position.

### 4.2.1 Fan Only

The 1D energy spectra $E_{11}(\kappa)$ for each probe plotted against wavenumber $\kappa = 2\pi/l = 2\pi f/\bar{U}$ can be found in Figures 4.3, 4.4 and 4.5 for the film, traditional and mini probes respectively. This wavenumber relation takes advantage of Taylor's frozen turbulence hypothesis, where data taken in terms of time can

Table 4.1: Air and $SF_6$ Flow Speed Properties

| Property | Film | | Traditional | | Mini | |
|---|---|---|---|---|---|---|
| | Low | High | Low | High | Low | High |
| $Re_{\lambda a}$ | 380 | 983 | 385 | 943 | 353 | 1005 |
| $Re_{\lambda s}$ | 375 | 1060 | 351 | 1140 | 325 | 1064 |
| $M_{ta}$ | 0.007 | 0.046 | 0.007 | 0.056 | 0.007 | 0.053 |
| $M_{ts}$ | 0.018 | 0.116 | 0.015 | 0.171 | 0.016 | 0.149 |
| $\eta_a$ [$\mu$m] | 63.9 | 15.2 | 65.7 | 13.2 | 65.5 | 13.7 |
| $\eta_s$ [$\mu$m] | 62.3 | 15.4 | 71.2 | 11.6 | 68.4 | 12.8 |

be put in terms of distance by $x = \bar{U}t$. Taylor's hypothesis is valid for low turbulence intensities, and was found to be valid on-axis of a turbulent jet where the jet has reached self-similarity and its departure from local isotropy is small [40]. Moreover, the energy spectra were validated assuming:

$$\int E_{11}(\kappa)d\kappa = \left\langle u_1^2 \right\rangle$$

Each energy spectra figure has a plot of both air and $SF_6$ at low and high speed settings, the $Re_\lambda$ and $M_t$ values for which can be found in Table 4.1. The black dashed line shows the wavenumber corresponding to the hot wire's sensing length. A larger mean velocity introduced larger amounts of turbulent kinetic energy into the flow and caused the spectra for all $\kappa$ to shift upwards, which was why the high speed setting had significantly more energy than the low speed setting. Slight deviations in the mean flow velocity changed the relative magnitude of the spectra, most noticeably at the large scales (small $\kappa$).

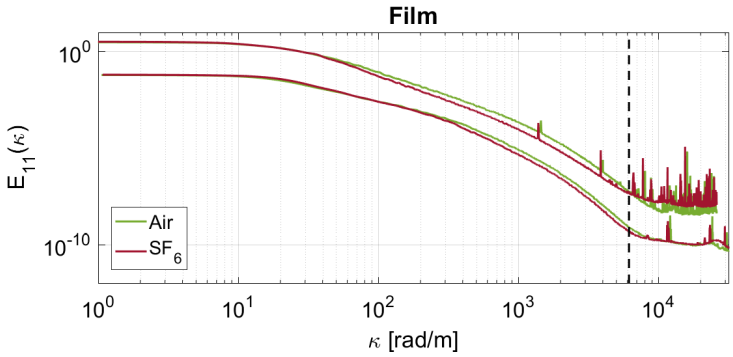


Figure 4.3: Energy Spectra of Film Probe

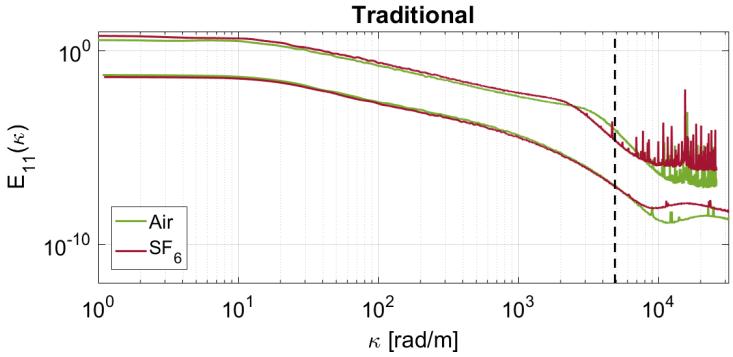


Figure 4.4: Energy Spectra of Traditional Probe

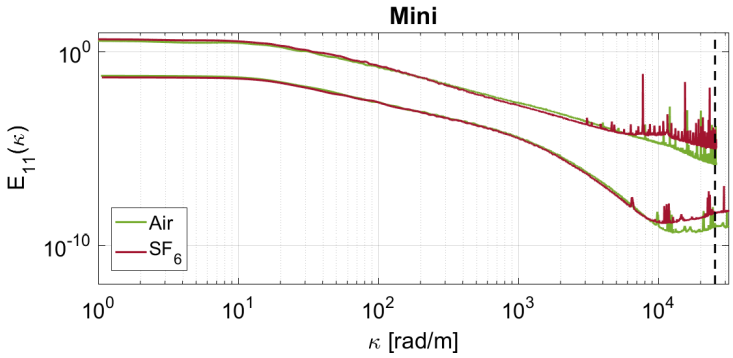


Figure 4.5: Energy Spectra of Mini Probe

The calculated Kolmogorov scales $\eta = (\nu^3/\varepsilon)^{1/4}$ are also shown in Table 4.1 for comparison. The Kolmogorov scale estimates were compromised by

the probes' spatial filtering since the sensing lengths of all three probes were larger [41]. The effects from spatial filtering could be seen in the drastically decreasing energy spectra at high wavenumbers, especially for the high speed condition. The attenuated energy spectra gives the incorrect impression that the dissipation range begins close to $\kappa \sim 1 \times 10^3$ for the film probe, and close to $\kappa \sim 2.5 \times 10^3$ for the traditional probe. Note that this $\kappa$ is just before the wavenumber corresponding to the traditional probe length.

The smaller sensing length of the mini probe did not spatially filter the data to the same degree, and was able to better resolve smaller scales as shown by the extension of the inertial range far past $\kappa \sim 1 \times 10^4$, where the anemometer noise level begins. Both the dissipation range and sensing length were buried within the anemometer noise level. Since the upper frequency of the turbulence measurement was determined by the anemometer frequency response [33], an anemometer with a faster frequency response and smaller probe would be needed to resolve the entire inertial and dissipation range at the high speed setting. The mini probe low speed condition was the only dissipation range that was resolvable, beginning near $\kappa \sim 1 \times 10^3$

The inertial range for turbulent flows:

$$E_{11}(\kappa) = C\varepsilon^{2/3}\kappa^{-n_1}$$

where $n_1$ is the inertial range scaling power coefficient and $C$ is a universal constant typically take to be $C = 1.5$ [36, 42]. The dissipation in compressible turbulent flows has a higher value, particularly near shocklets, as compared to that in incompressible turbulence [43]. The compressibility effects act as a source of dissipation in addition to viscous dissipation [42]. Compressible turbulent inertial range scaling $0n_1 = 2$ typically only holds for the compressive

component of the velocity from the Helmholtz decomposition, whereas the entire energy spectra including the compressive component follows the $n_1 = 5/3$ scaling [44, 45, 42]. However, the 2 inertial scaling can be seen for the entire energy spectra for the high speed $SF_6$ case.

Figure 4.6 shows the change in the inertial range scaling from low to high Reynolds and Mach Numbers as compared to the Mydlarski and Warhaft data [46]. The 95% confidence intervals were based on the bootstrap uncertainty method. The inertial range scaling $n_1$ started below the typical incompressible 5/3 scaling for undeveloped turbulence, but increased with increasing $Re_\lambda$ to 5/3. The air case hovered around 5/3 for higher $Re_\lambda$ but continued to increase for $SF_6$. When plotted against turbulent Mach Number, the data collapsed for low $M_t$. Because the $FS_6$ case extended to higher $M_t$, the scaling coefficient $n_1$ continued to increase towards the compressible 2 scaling values. Hence, the $SF_6$ case tended towards compressibility while the air case remained incompressible.

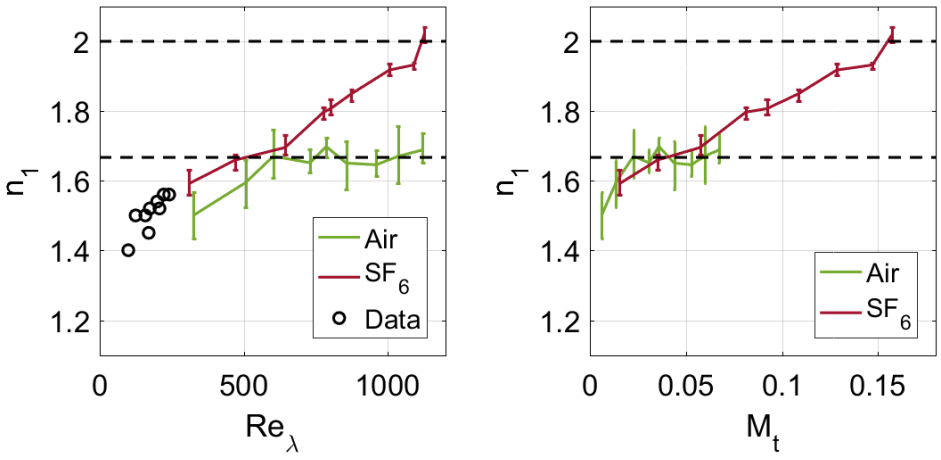


Figure 4.6: Energy Spectra Inertial Range Scaling

### 4.2.2 Fan and Speakers

The following graphs show the energy spectra as measured by the mini probe, since this probe had the smallest sensing length and therefore minimal spatial filtering and high temporal resolution. The speakers were driven with SPL given in Table 3.1. The energy spectra are plotted against frequency instead of wavenumber to highlight the alignment between speaker driving frequency and flow frequency.

An increasingly larger pocket of energy at each speaker forcing frequency for the low speed $SF_6$ case can be seen for the 111Hz, 202Hz and 318Hz energy spectra in Figures 4.7, 4.8, and 4.9 respectively. The figure insets show the low speed condition peaks more closely. Since the fan solenoidal turbulence had higher energy content at low frequencies, the speaker-contributed energy for lower forcing frequencies was buried within the fan energy spectra. The energy pocket was easier to discern at high frequencies since the fan turbulent energy was less. The energy pocket could also be seen within the energy spectra ratio graph. The 318Hz forcing frequency spectra was the only instance to show a peak for the high speed $SF_6$ case, seen in Figure 4.9.

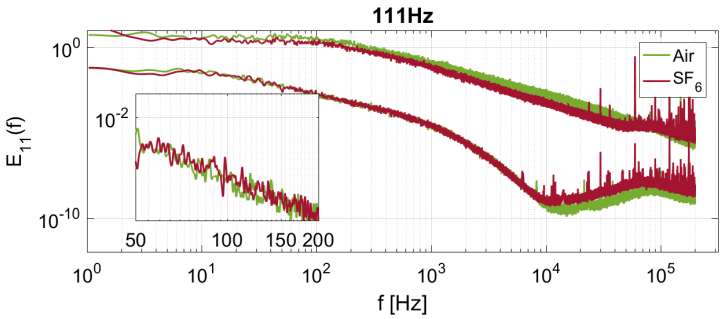


Figure 4.7: Energy Spectra at 111Hz

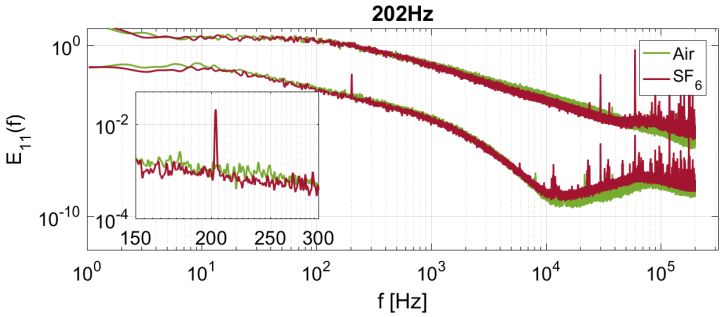


Figure 4.8: Energy Spectra at 202Hz

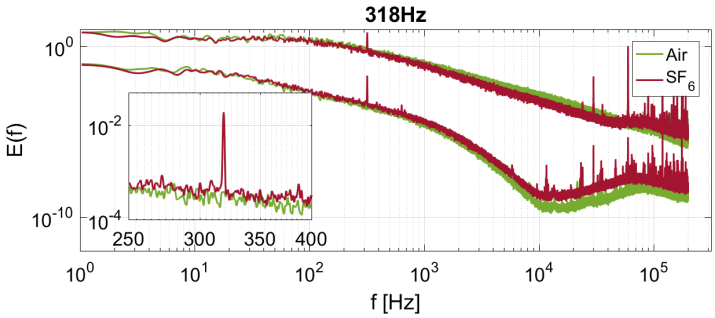


Figure 4.9: Energy Spectra at 318Hz

The 814Hz spectra show both air and $SF_6$ cases detected energy at the resonant frequency as well as at higher order resonant modes, seen in Figure 4.10. These peaks occurred at the frequencies $f_{res}$ indicated in Table 4.2, which shows how closely $f_{res}$ matches the calculated higher order frequencies $f_{calc}$. While the lower forcing frequencies had a negligible effect on the air case, the air case experienced these resonating frequency effects, indicating either the flow was excited or the hot wire was vibrating with the T-RExE.

Table 4.2: Resonant Frequency Modes

| Resonant Mode | 1 | 2 | 5 | 7 | 9 |
|---|---|---|---|---|---|
| $f_{calc}$ [Hz] | 814 | 1628 | 4070 | 5698 | 7326 |
| $f_{res}$ [Hz] | 814 | 1628 | 4070 | 5698 | 7327 |

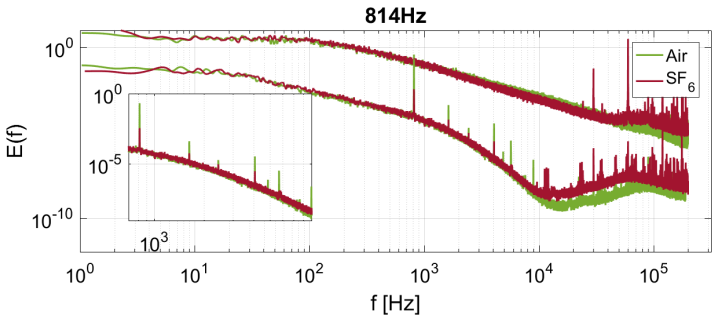


Figure 4.10: Energy Spectra at 814Hz

For the low speed 6860/2704Hz frequency setting, a single peak could be seen for $SF_6$ at its frequency, and a broader peak for air at its frequency, seen in Figure 4.11. A small peak could be seen only for the air high speed condition, suggesting any interaction between the forcing frequency and the flow was below the fan energy. Since the air case was again excited at its speaker frequency, it can be assumed the hot wire probe was structurally vibrating with the pressure vessel.

All energy spectra figures showed faster decreasing amounts of energy at high wavenumbers for the high speed $SF_6$ case compared to the air case. This phenomena was consistent with a higher power scaling in the inertial range, indicative of compressibility effects at work.

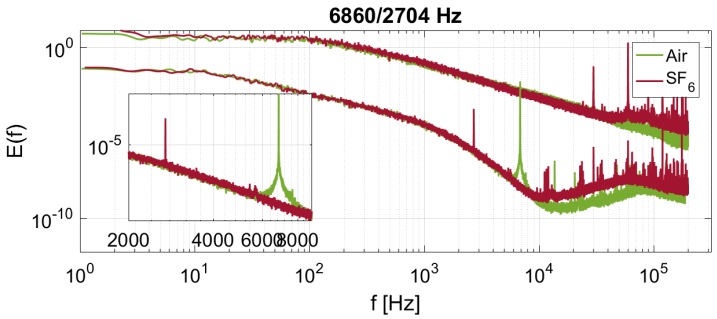


Figure 4.11: Energy Spectra at 6860/2704Hz

## 4.3 Velocity Derivative PDFs

Skewness of the velocity derivative is:

$$S = \frac{\left\langle (du_1/dx_1)^3 \right\rangle}{\left\langle (du_1/dx_1)^2 \right\rangle^{3/2}}$$

where the values are typically negative and its absolute value increasing with $Re_\lambda$ [36]. Velocity derivative skewness as measured by the mini probe is shown in Figure 4.12 with a 95% confidence interval denoted by errorbars calculated using Student's t-distribution.

Both gases increased to a plateau at $-S = 0.3$ for air and $-S = 0.25$ for $SF_6$. However, typically jets reached $-S = 0.4$ for this range of $Re_\lambda$ [47]. Poor spatial and temporal resolution of the hot wire probe and associated equipment adversely affected the skewness estimate, causing the skewness to be underestimated [48]. As aforementioned, the hot wire probes were orders of magnitude larger than the Kolmogorov scale, and thus the hot wire probes cannot resolve all the small scale velocity fluctuations.

The absolute value of the skewness for both air and $SF_6$ increased up to $Re_\lambda \sim 600$ before decreasing again. Tabeling et al found a similar decreasing

skewness after $Re_\lambda \sim 800$ [49]. At this point, the turbulence might have transitioned to a different state or the skewness behavior became nonuniversal [49].

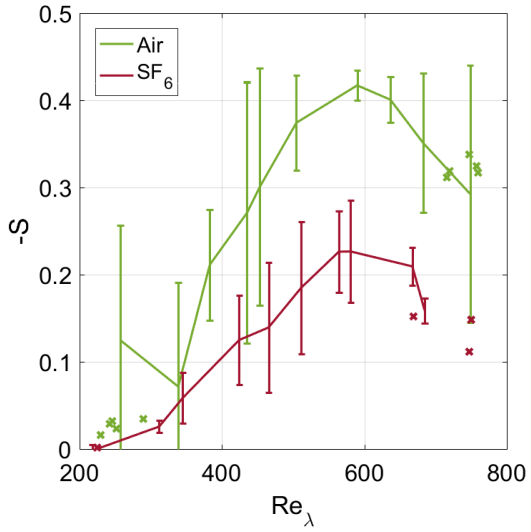


Figure 4.12: Velocity Derivative Skewness of Mini Probe

Past $Re_\lambda \sim 350$, $SF_6$ skewness values deviated below air skewness values. Typically, compressibility decreases the absolute value of the skewness [50], as seen in the $SF_6$ case at the same $Re_\lambda$ as compared to air.

The 'x' plotted in Figure 4.12 denote the velocity derivative skewness values at different speaker forcing frequencies. The points generally follow the trend of the fan, showing this additional fluid forcing motion had no significant impact on the velocity derivative skewness. Once again it can be seen that the speaker forcing did not interact with the fan flow motions.

# CHAPTER 5

# CONCLUSION

In conclusion, the experimental equipment was successfully used to maintain the large scale turbulence dynamics, as seen in the power, axial and radial profiles, between air and $SF_6$ without changing the boundary conditions. Using gases with similar dynamic viscosities and adjusting the pressures of each case so the kinematic viscosities matched enabled flow measurements to be taken at the same pressure vessel location where Reynolds Number remained the same. The integral length remained the same for all test cases, while the Taylor length scales followed the same trend with $u'$, and thus $Re_\lambda$, for both air and $SF_6$.

Changing the gas affected the small scale dynamics as determined by the 1D energy spectra. The energy spectra demonstrated compressible scaling at the high speed cases for $SF_6$, while the air case remained within the incompressible scaling regime at the same $Re_\lambda$. However the limited spatial resolution of the hot wire probe and temporal resolution of the anemometer limited the highest scales that could be measured in the flow. In future, smaller probes, such as tiny probes or NSTAPs, optimized with a higher frequency response anemometer are needed to resolve down to the Kolmogorov scales present in the high speed flows. Additionally, the influence of the speakers on the flow was limited to the particular speaker forcing frequency as noted in the frequency content. Perhaps using a randomized speaker forcing frequency pattern or multiple frequencies simultaneously will enable the speaker forcing to better interact with the solenoidal fan flow.

Increasing negative skewness values with $Re_\lambda$ of both air and $SF_6$ demonstrated the high turbulence phenomena present in the flow. Lower absolute

value of the skewness for $SF_6$ at the same $Re_\lambda$ indicated compressibility effects at work. The underestimated skewness values as compared to typical jet flow denote the spatial filtering present in the flow, as the probe did not catch all the velocity fluctuations at the small scales. As mentioned above, a higher resolution equipment setup is necessary to resolve these small scales at the high speeds.

The development of experimental methods to measure compressible flow fields is crucial to the advancement of aerodynamic designs and analyses as well as to our understanding of galactic star formations. Experimental data will not only provide measured realistic values to be integrated into simulation technologies, but also further explain the scientific phenomena observed in aerospace and astrophysical studies.

## BIBLIOGRAPHY


[1] Peter Jordan and Tim Colonius. Wave packets and turbulent jet noise. *Annual Review of Fluid Mechanics*, 45:173–195, 2013.

[2] Joseph W. Nichols, Sanjiva K. Lele, Frank E. Ham, Steve Martens, and John T. Spyropoulos. Crackle noise in heated supersonic jets. *Journal of Engineering for Gas Turbines and Power*, 135(5), 2013.

[3] Rainer Friedrich. Compressible turbulent flows: Aspects of prediction and analysis. *ZAMM Zeitschrift Fur Angewandte Mathematik Und Mechanik*, 87(3):189–211, 2007.

[4] L. D. Kral. Recent experience with different turbulence models applied to the calculation of flow over aircraft components. *Progress in Aerospace Sciences*, 34(7):481–541, 1998.

[5] Thomas B. Gatski and Jean-Paul Bonnet. Compressibility, turbulence and high speed flow. *Academic Press*, 2013.

[6] Bruce G. Elmegreen and John Scalo. Interstellar turbulence: Observations and processes. *Annual Review of Astronomy and Astrophysics*, 42(1):211–273, 2004.

[7] Alexei G. Kritsuk, Michael L. Norman, Paolo Padoan, and Rick Wagner. The statistics of supersonic isothermal turbulence. *Astrophysics Journal*, 665(1):416–431, 2007.

[8] Sébastien Galtier and Supratik Banerjee. Compressible turbulence in astrophysics. *Société Française d'Astronomie et d'Astrophysique*, 2011.

[9] Christoph Federrath. On the universality of supersonic turbulence. *Monthly Notices of the Royal Astronomical Society*, 436(2):1245–1257, 2013.

[10] Shiyi Chen, Zhenhua Xia, Jianchun Wang, and Yantao Yang. Recent progress in compressible turbulence. *Acta Mech Sin*, 31(3):275–291, 2015.

[11] Ravi Samtaney, D. I. Pullin, and Branko Kosović. Direct numerical simulation of decaying compressible turbulence and shocklet statistics. *Physics of Fluids*, 13, 2001.

[12] Max M. Munk and Elton W. Miller. The variable density wind tunnel of the national advisory committee for aeronautics. 1926.

[13] E. von Doenhoff and F. T. J. Abbott. The langley two-dimensional low-turbulence pressure tunnel. 1947.

[14] C. Pankhurst. *Nature*, 238(375), 1972.

[15] B. Gölling and O. Erne. Experimental investigation on periodic rolling of a delta wing flow at transonic mach numbers. *Notes on Numerical Fluid Mechanics and Multidisciplinary Design (NNFM)*, 92, 2006.

[16] Christian Klein. Application of pressure sensitive paint (psp) for the determination of the instantaneous pressure field of models in a wind tunnel. *Aerospace Science and Technology*, 4:103–109, 2000.

[17] N. A. Buchmann, Y. C. Kücükosman, K. Ehrenfried, and C. J. Kähler. Wall pressure signature in compressible turbulent boundary layers. *ERCOFTAC*, 23:93–102, 2016.

[18] G. Briassulis, J. H. Agui, J. Andreopoulos, and C. B. Watkins. A shock tube research facility for high-resolution measurements of compressible turbulence. *Experimental Thermal and Fluid Science*, 13(4):430–446, 1996.

[19] Y. Andreopoulos. Vorticity and velocity alignment in compressible flows: An experimental study of helicity density in turbulence and vortices. *Russian Journal of Electrochemistry*, 44(4):422–428, 2008.

[20] C. B. Millikan, J. E. Smith, and R. W. Bell. *Journal of Aeronautics*, 15(69), 1948.

[21] V. Zagarola and A. J. Smits. *Physics of Fluids*, 78(239), 1997.

[22] E. Bodenschatz, G.P Bewley, H. Nobach, M. Sinhuber, and H. Xu. Variable density turbulence tunnel facility. *Review of Scientific Instruments*, 85(9), 2014.

[23] *Perry's Chemical Engineers' Handbook*. McGraw-Hill Co., sixth edition, 1984.

[24] M & M Control Service. *Safety and Relief Valves*.

[25] Gregory P. Bewley, Kelken Chang, and Eberhard Bodenschatz. On integral length scales in anisotropic turbulence. *Physics of Fluids*, 24, 2012.

[26] Validyne Engineering Corporation. *Instruction Manual: CD23 Digital Transducer Indicator*.

[27] Hans Rottländer, Walter Umrath, and Gerhard Voss. *Fundamentals of leak detection*. Leybold Corporation.

[28] Vishal D. Chaudhari and Avinash D. Desai. Performance evaluation of vacuum system: Pump-down time. *International Journal of Scientific and Engineering Research*, 2(11), 2011.

[29] A. Berman. Water vapor in vacuum systems. *Vacuum*, 47(4), 1995.

[30] CPS Products. *Refrigerant Leak Detector: Owner's Manual*.

[31] Direct global warming potentials. *Intergovernmental Panel on Climate Change*, 2007.

[32] J. Mi, M. Xu, and T. Zhou. Reynolds number influence on statistical behaviors of turbulence in a circular free jet. *Physics of Fluids*, 25, 2013.

[33] A. J. Smits, K. Hayakawa, and K. C. Muck. Constant temperature hot-wire anemometer practice in supersonic flows. *Experiments in Fluids*, 83, 1983.

[34] Sean C. C. Bailey, Gary J. Kunkel, Marcus Hultmark, Margit Vallikivi, Jeffrey P. Hill, Karl A. Meyer, Candice Tsay, Craig B. Arnold, and Alexander J. Smits. Turbulence measurements using a nanoscale thermal anemometry probe. *Journal of Fluid Mechanics*, 663:160–179, 2010.

[35] Michael Sinhuber, Eberhard Bodenschatz, and Gregory P. Bewley. Decay of turbulence at high reynolds numbers. *Physical Review Letters*, 114, 2015.

[36] Stephen B. Pope. *Turbulent Flows*. Cambridge University Press, 2000.

[37] R. A. Antonia, B. R. Satyaprakash, and A. K. M. F. Hussain. Measurements of dissipation rate and some other characteristics of turbulent plane and circular jets. *Physics of Fluids*, 23(695), 1980.

[38] M. Xu1, J. Zhang, J. Mi, and A. Pollard. Local dissipation scales in turbulent jets. In *20th Australasian Fluid Mechanics Conference*, 2016.

[39] Hamed Sadeghi, Philippe Lavoie, and Andrew Pollard. Effects of finite hot-wire spatial resolution on turbulence statistics and velocity spectra in a round turbulent free jet. *Experiments in Fluids*, 59, 2018.

[40] J. Mi and R. A. Antonia. Corrections to taylor's hypothesis in a turbulent jet. *Physics of Fluids*, 6, 1994.

[41] A. Ashok, S. C. C. Bailey, M. Hultmark, and A. J. Smits. Hot-wire spatial resolution effects in measurements of grid-generated turbulence. *Experimental Fluids*, 53:1713–1722, 2011.

[42] Bohua Sun. The spatial scaling laws of compressible turbulence. *Applied Mathematics and Mechanics*, 38(6), 2017.

[43] Sangsan Lee, Sanjiva K. Lele, and Parviz Moin. Eddy shocklets in decaying compressible turbulence. *Physics of Fluids*, 3(657), 1991.

[44] Jianchun Wang, Yantao Yang, Yipeng Shi, Zuoli Xiao, X. T. He, and Shiyi Chen. Cascade of kinetic energy in three-dimensional compressible turbulence. *Physical Review Letters*, 110, 2013.

[45] Jianchun Wang, Toshiyuki Gotoh, and Takeshi Watanabe. Shocklet statistics in compressible isotropic turbulence. *Physical Review Letters*, 2, 2017.

[46] L. Mydlarski and Z. Warhaft. On the onset of high-reynolds-number grid-generated wind tunnel turbulence. *Journal of Fluid Mechanics*, 320:331–368, 1996.

[47] H. Fellouah and A. Pollard. The velocity spectra and turbulence length scale distributions in the near to intermediate regions of a round free turbulent jet. *Physics of Fluids*, 21(11), 2009.

[48] Paolo Burattini, Philippe Lavoie, and Robert A. Antonia. Velocity derivative skewness in isotropic turbulence and its measurement with hot wires. *Experimental Fluids*, 45:523–535, 2008.

[49] K. R. Sreenivasan and R. A. Antonia. The phenomenology of small-scale turbulence. *Annual Review of Fluid Mechanics*, 29:435–472, 1997.

[50] S. Pirozzoli and F. Grasso. Direct numerical simulations of isotropic compressible turbulence: Influence of compressibility on dynamics and structures. *Physics of Fluids*, 16(12), 2004.